



Revealing the Antiviral Activity of Certain Volatile Oils against Respiratory RNA and DNA Viruses Supported by Molecular Dynamics Analysis



Mohamed S. Refaey^{1,2,*}, Omnia Kutkat³, Yassmin Moatasim³, Nahla Sameh Tolba⁴, Anis Zaid⁵, Ahmed M. Elshorbagy¹, Khloud Nassar⁶, Ahmed A. El-Rashedy^{7,10}, Mohamed F. El-Badawy⁸, Khaled A. M. Abouzid⁹, Marwa A. A. Fayed¹ and Yaseen A. M. M. Elshaier¹⁰

¹Department of Pharmacognosy, Faculty of Pharmacy, University of Sadat City, Menoufia 32897, Egypt

²Department of Pharmacognosy and natural products, Faculty of Pharmacy, Menoufia National University, km Cairo-Alexandria Agricultural Road, Menoufia, Egypt

³Center of Scientific Excellence for Influenza Viruses, National Research Centre (NRC), Giza 12622, Egypt

⁴Department of Pharmaceutics, Faculty of Pharmacy, University of Sadat City, Menoufia 32897, Egypt

⁵Department of Pathology, faculty of Veterinary Medicine, University of Sadat City, Egypt

⁶Department of biochemistry, Faculty of Pharmacy, University of Sadat City, Menoufia 32897, Egypt

⁷Department of The Chemistry of Natural and Microbial Products, Pharmaceutical and Drug Industries Institute, National Research Centre (NRC), 33 El-Behouth St., Dokki, Giza, 12622, Egypt.

⁸Microbiology and immunology Department, Faculty of Pharmacy, University of Sadat City, Menoufia 32897, Egypt

⁹Pharmaceutical Chemistry Department, Faculty of Pharmacy, Ain Shams University, Abbassia 11566, Cairo, Egypt

¹⁰Department of Organic and Medicinal Chemistry, Faculty of Pharmacy, University of Sadat City, Menoufia 32897, Egypt

Abstract

An important obstacle to antiviral therapy is the emergence of drug-resistant virus strains. So, it is vital to find new alternatives with robust activity and great safety. In this study, eight volatile oils (VOs) were evaluated for their cytotoxic and antiviral activity against respiratory RNA (H1N1, H5N1, SARS-CoV-2) and DNA (HSV) viruses. The results revealed that *Coriandrum sativum* and *Pimpinella anisum* VOs had antiviral activity against avian influenza A (H5N1) virus (IC₅₀s of 8.11, 13.71 µg/mL, respectively) and influenza A (H1N1) virus (IC₅₀s of 7.11, 1.67 µg/mL, respectively). Also, *P. anisum* VO exhibited noticeable antiviral activity against herpes simplex virus (HSV) with IC₅₀ 18.28 µg/mL, while *Rosmarinus officinalis* and *P. anisum* VOs were effective against severe acute respiratory syndrome coronavirus 2 (SARS-CoV-2) with IC₅₀s of 3.078 and 4.66 µg/mL, respectively. The study investigated the proposed mechanism of the effective VOs (*P. anisum*, *C. sativum*, and *R. officinalis*) against SARS-CoV-2 molecular targets: papain-like protease (PLpro), angiotensin-converting enzyme 2 (ACE2), and spike protein. The major identified compounds in the potent VOs were docked to PLpro, ACE2, and spike protein to reveal their mechanism of action on the enzymatic level. The molecular docking study revealed that anethole; a major component of *P. anisum*, exhibited a strong binding affinity towards SARS-CoV-2 PLpro and showed a unique binding mode against the SARS-CoV-2 spike protein compared to other major VO components. Molecular dynamic simulation revealed that anethole selectively targets the catalytic active site of the SARS-CoV-2 spike receptor, the CoV spike (S) glycoprotein receptor, and the SARS-CoV-2 papain-like protease. This is the first report examining these VOs' antiviral efficacy against certain respiratory RNA and DNA viruses. It also explains the possible mechanistic study of the most active VOs on SARS-CoV-2.

Keywords: Anethole, Anise, Molecular dynamic, Molniravir, Rosemary, SARS-CoV-2.

1. Introduction

Globally, respiratory infections are the leading cause of death [1]. Across the world, there were 2.4 million deaths from lower respiratory infections in 2019, and 488 million incident cases [2]. As reported by WHO 2021, lower respiratory infections are still the deadliest transmissible disease in the world and the fifth biggest cause of mortality [3]. Young children can make up to 60% of visits to practitioners and approximately 25% of hospital admissions [4]. Most respiratory virus infections are self-restricting and only affect the upper airways [5], while in vulnerable individuals, the symptoms might affect the lower airways, causing wheezing, breathing difficulties, pneumonia, or bronchiolitis [6]. Common respiratory viral infections include adenovirus, enteric viruses, influenza, parainfluenza, rhinovirus, human coronavirus, human metapneumovirus, and

*Corresponding author e-mail: mohamed.said@fop.usc.edu.eg; (Mohamed S. Refaey).

Received date 23 March 2025; Revised date 05 April 2025; Accepted date 03 May 2025

DOI: 10.21608/ejchem.2025.370688.11501

©2025 National Information and Documentation Center (NIDOC)

respiratory syncytial virus [7]. Severe influenza syndrome, including fever, coughing, dyspnea, and radiological signs of pneumonia, is the hallmark of human H5N1 infection [8, 9]. Acute respiratory distress syndrome is assumed to be connected to most patients' deaths from progressive respiratory failure [10, 11]. As of February 2023, the novel coronavirus known as SARS-CoV-2 is the cause of the COVID-19 pandemic, which has claimed the lives of nearly 6 million people globally [12]. The illness can present with a broad range of clinical symptoms, from common cold symptoms like fever, headaches, and coughing to life-threatening conditions like pneumonia, failure of several organs, and death [13]. The government started a vaccination program to curb the spread of viruses, but there are several problems with vaccine manufacturing since new virus varieties, such as influenza and coronaviruses, are constantly being created by virus reassortment, which makes vaccines unable to offer complete protection. Furthermore, children, the elderly, and those with weakened immune systems should not receive vaccinations; therefore, there is a pressing need for antiviral drugs that can handle many infections [14, 15]. Researchers are still investigating possible antiviral medications, specifically for COVID-19, for which various protocols have established antiviral treatments (such as molnupiravir and remdesivir), monoclonal antibody therapy, and symptomatic therapies like antipyretics, anticoagulants, and corticosteroids [16]. Because of the pandemic nature of these viruses, especially with the introduction of the SARS-CoV-2 Omicron variant, it is now more difficult to address this public health concern. Therefore, complementary and alternative approaches should be investigated [17].

Researchers all around the globe are interested in VOs because of their potential value in treating respiratory tract illnesses caused by diverse bacterial and viral strains [16, 18, 19]. Strong antiviral action of VOs has been demonstrated against a variety of viruses, including avian influenza, coronavirus, influenza virus, human immunodeficiency virus, human herpes viruses (HSV1 and HSV2), and yellow fever virus [19-21]. Additionally, the phytochemicals present in VOs are potential candidates with a wide spectrum of medicinal activity. Anethole, carvacrol, cinnamaldehyde, cinnamyl acetate, geraniol, l-4-terpineol, pulegone, and thymol are among the monoterpenes, phenolic terpenoids, and phenylpropanoids that have been found to be strong antiviral substances and that can block the viral spike protein *in vitro* [22]. A number of clinical trials were carried out to assess the effectiveness of VOs as an additional medicine for the therapy of COVID-19, according to recent studies [23-25].

As a part of our ongoing investigation into potential naturally derived drug templates and following international guidelines for green urbanization to avoid the side effects and precautions of synthetic compounds for the treatment of respiratory tract infections caused by viruses, particularly anti-SARS-CoV-2 [26] and influenza viruses, we have selected eight medicinal herbs that are easily obtained from both commercial and farmed sources. Here, the hydrodistillation method was used to extract the volatile oils (VOs) from these specific plants. The VOs were tested for their *in vitro* cytotoxic and antiviral activity against specific respiratory RNA viruses (human influenza H1N1, avian influenza H5N1, and SARS-CoV-2) and DNA viruses (Herpes simplex virus (HSV) type 1) (Fig. 1). The approach of gas chromatography-mass spectrometry (GC-MS) was used to examine the chemical profiling of the potent VOs. The mechanism of action of the most effective VOs, along with some of their main constituents, was especially studied against the molecular targets of SARS-CoV-2, namely spike protein, ACE2, and PLpro. Through investigations using molecular docking, molecular dynamic simulation, and experimentation, the potential enzymatic mode of action of antivirals was explored.

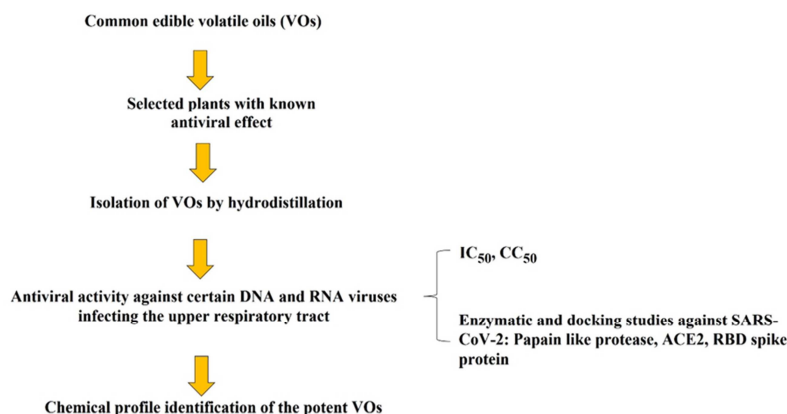


Figure 1: Rationale of the current work

2. Material and methods

2.1. Plant material

In this investigation, eight plants were used (Table 1). Some were obtained from the Experimental Plants Station, Cairo University, Cairo, Egypt, while others were bought from the herbal commercial marketplace in September 2021, Cairo, Egypt. Dr. Mohamed Azzazy, a professor of plant ecology at the Surveys of Natural Resources Department, Environmental Studies and Research Institute, University of Sadat City, Egypt, verified the plant species. The Environmental Studies and Research Institute's herbarium in Sadat City, Egypt, is home to the voucher specimens.

Table 1: The botanical names, locations where they were collected, and voucher numbers of the plants used in this work

Scientific name	Family	Common name	Part used	Voucher No.	Site of collection
<i>Citrus sinensis</i>	Rutaceae	<i>Citrus</i>	<i>Peels</i>	Cs-En-USC-11	HCM*, Cairo, Egypt
<i>Artemisia cina</i>	Asteraceae	<i>Santonica</i>	<i>Flowers</i>	Ac-En-USC-12	HCM, Cairo, Egypt
<i>Coriandrum sativum</i>	Apiaceae	<i>Coriander</i>	<i>Fruits</i>	Cs- En-USC-13	HCM, Cairo, Egypt
<i>Lavandula officinalis</i>	Lamiaceae	<i>Lavander</i>	<i>Flowers</i>	Lo-En-USC-14	HCM, Cairo, Egypt
<i>Pimpinella anisum</i>	Apiaceae	<i>Anise</i>	<i>Fruits</i>	Pa-En-USC-15	HCM, Cairo, Egypt
<i>Cymbopogon citratus</i>	Poaceae	<i>Lemon grass</i>	<i>Aerial parts</i>	Cc-En-USC-16	Cairo University, Cairo, Egypt
<i>Rosmarinus officinalis</i>	Lamiaceae	<i>Rosemary</i>	<i>Aerial parts</i>	Ro-En-USC-17	Cairo University, Cairo, Egypt
<i>Thymus vulgaris</i>	Lamiaceae	<i>Thyme</i>	<i>Aerial parts</i>	Tv-En-USC-18	Cairo University, Cairo, Egypt

*HCM, Herbal commercial market

2.2. Preparation of Essential Oil

A weight of 250 g of each pulverized plant part (as listed in Table 1) was subjected to hydrodistillation and VO isolation as reported in [27].

2.3. Cell lines and viruses

Dulbecco's Modified Eagle's Medium (Lonza, Basel, Germany) (DMEM) supplemented with 10% inactivated fetal bovine serum (FBS) (Gibco, Waltham, MA, USA) and 1% of a combination of antibiotic-antimycotic (Gibco) was used to maintain Madin Darby Canine Kidney (MDCK), VERO E6 cells, and VERO cells (ATCC No. CRL-1586). The Vero lineage was isolated from kidney epithelial cells extracted from an African green monkey (*Chlorocebus sp.*). The cell lines were authenticated within 3 years of use in experiments, and they have been tested for mycoplasma contamination. The cells grew at 37 °C in 5% CO₂. Influenza A virus A/California/04/2009 (H1N1, H1N1pdm09) and highly pathogenic A/chicken/Egypt/B13825A/2017 (H5N1 wild, clade 2.2.1.2) were employed in this investigation. For 48 hours, both viruses were grown in specific pathogen-free embryonated chicken eggs (SPF-ECEs) that were 11 days old. The hemagglutination (HA) assay, the 50% tissue culture infectious dose assay (TCID₅₀/mL), and the 50% egg infectious dose assay (EID₅₀/mL) were used to titrate the propagated viruses. In this work, the Egyptian Centre of Scientific Excellence for Influenza Viruses, National Research Centre, gave the *Herpes simplex* virus type 1. The COVID-19 disease hCoV-19/Egypt/NRC-03/2020 (NRC-03-nhCoV) is caused by SARS-CoV-2 (Accession Number on GSAID: EPI_ISL_430820).

2.3.1. Cytotoxicity assay on cells:

In vitro cytotoxicity assay to determine the cytotoxic concentration of 50% (CC₅₀) of each oil on different cell lines: [28]

The test VOs were generated in stock solutions in 10% DMSO in ddH₂O, and these solutions were then further diluted to the working solutions using DMEM to ascertain the half maximum cytotoxic concentration (CC₅₀). Using slightly modified versions of the 3-(4, 5-dimethylthiazol-2-yl)-2, 5-diphenyltetrazolium bromide (MTT) technique, the cytotoxic activity of the VOs was assessed in MDCK, VERO E6, and VERO cells. In summary, the cells were seeded at a density of 3×10⁵ cells/mL in 96-well plates with 100 µL of CO₂ per well, and they were incubated for 24 hours at 37 °C. Cells were exposed to different doses and serial dilutions of the tested VOs in triplicate after 24 hours.

Following a 24-hour incubation period, the supernatant was disposed of, and the cell monolayers underwent three rounds of washing with sterile 1x phosphate-buffered saline (PBS), and each well received an MTT solution (20 µL of 5 mg/mL stock solution). The medium was then aspirated after four hours of incubation at 37 °C. 200 µL of acidified isopropanol (0.04 M HCl in 100% isopropanol = 0.073 mL HCl in 50 mL isopropanol) was used to dissolve the formazan crystals that had been generated in each well. The absorbance of formazan solutions at λ_{max} 540 nm was measured using a multi-well plate reader, with 620 nm as a reference wavelength.

2.3.2. Antiviral activity:

2.3.2.1. Inhibitory concentration 50% (IC₅₀):

2.4×10⁴ MDCK cells for the influenza viruses H5N1 and H1N1, Vero E6 cells for the SARS-CoV-2 virus, and VERO cells for herpes simplex were evenly distributed in each well of 96-well tissue culture plates. The plates were then incubated for an entire night at 37 °C in a humidified incubator with 5% CO₂. Following a single wash with 1x PBS, the cell monolayers were then exposed to serial dilutions from VOs mixed with the viruses B13825A (H5N1), SARS-CoV-2, and Herpes simplex based on the TCID₅₀ concentration for each one separately for one hour in an incubator with 5% CO₂ that was humidified to 37 °C. On top of the cell monolayers, 100 µL more of DMEM was added. After being incubated for 72 hours at 37 °C in an incubator with 5% CO₂, the cells were fixed for two hours with 50 µL of 10% paraformaldehyde and stained for fifteen minutes at room temperature using 1% crystal violet in distilled water. Next, 100 µL of 100% methanol per well was used to dissolve the crystal violet dye. An Anthos Zenyth 200rt plate reader (Anthos Labtec Instruments, Heerhugowaard, Netherlands) was used to measure the optical density of the color at 570 nm. The quantity required to cut the viral-induced cytopathic effect (CPE) by 50% in comparison to the virus control is known as the tested VOs' IC₅₀ [29, 30].

2.3.2.2. Papain-like protease (PLpro) inhibition assay

After dispensing 40 μ L of 142 nM PLpro in Buffer A [50 mM Hepes, pH 7.5; 0.1 mg/mL bovine serum albumin (BSA); and 5 mM dithiothreitol (DTT)] into each well, 10 μ L of the tested drug or VOs were incubated for five minutes. Following a vigorous 30-second shaking, 10 μ L of 250 μ M Arg-Leu-Arg-Gly-Gly-AMC (RLRGG-AMC) in Buffer A was added to start the reaction, which was then incubated for six minutes. After quenching the reactions with 10 μ L of 0.5 M acetic acid, shaking the mixture for 30 seconds, and measuring the intensity of the fluorescence emission (excitation λ : 360 nm; emission λ : 460 nm) [31]. The following medications were utilized as standard drugs: molniravir (donated by PHARCO Pharmaceuticals, New Borg El Arab City, Alexandria, Egypt), remdesivir (donated by PHARCO Pharmaceuticals, New Borg El Arab City, Alexandria, Egypt), hydroxychloroquine (donated by Future pharmaceutical industries, Cairo, Egypt), and anethole (donated by Averroes Pharma, Sadat City, Menoufia, Egypt).

2.3.2.3. Spike protein receptor binding domain (RBD) inhibition assay

Before being placed on a 96-well plate and blocked with 2% fat-free milk in PBS for two hours at 37 °C, SARS-CoV-2 and RBD (1 μ g/mL) were first incubated with the tested substance or VOs at 37 °C for two hours. After adding 100 μ L of sACE2 protein to the plates, they were incubated at 37 °C for two hours. Following four washings, the bound protein was detected for two hours at 37 °C using a goat antibody specific to hACE2 (0.5 μ g/mL, R&D system). This was followed by an hour-long incubation at the same temperature using a horseradish peroxidase (HRP)-conjugated anti-goat IgG antibody (1:5,000, Thermo Fisher Scientific). Substratum 3,3',5,5'-Tetramethylbenzidine (TMB) (Sigma, St. Louis, MO) was added to visualize the reaction, and H₂SO₄ (1 N) was used to stop it. The ELISA plate reader (Tecan, San Jose, CA) was utilized to quantify the absorbance at λ_{max} 450 nm (A450) [32].

2.3.2.4. Angiotensin-converting enzyme (ACE2) binding efficiency

The following criteria were used to evaluate the compounds' and/or VOs' angiotensin-converting enzyme binding efficiency: After adding 100 μ L of sACE2 protein to the plates, they were incubated for two hours at 37 °C with varying doses of the tested chemicals and/or VOs. The plates were then left to incubate overnight at 4 °C and blocked for two hours at 37 °C using 2% fat-free milk in PBST. Following four washings, the bound protein was identified by incubating with HRP-conjugated anti-goat IgG antibody (1:5,000, Thermo Fisher Scientific) for one hour at 37 °C after hACE2-specific goat antibody (0.5 μ g/mL, R&D system) was applied for two hours at that temperature. Substratum 3,3',5,5'-Tetramethylbenzidine (TMB) (Sigma, St. Louis, MO) was added to visualize the reaction, and H₂SO₄ (1 N) was used to stop it. The ELISA plate reader (Tecan, San Jose, CA) was utilized to quantify the absorbance at 450 nm λ_{max} (A450) [33].

2.4. Gas chromatography-mass spectrometry analysis (GC-MS)

At the Central Laboratories Network, National Research Centre, Cairo, Egypt, a mass spectrometer detector (5977A) and gas chromatograph (7890B) were fitted with an Agilent Technologies GC-MS system. A DB-624 column (30 m x 320 μ m internal diameter and 1.8 μ m film thickness) was fitted to the GC. The following temperature program, an injection volume of 1 μ L, a split ratio of 1:10, and hydrogen as the carrier gas were used in the analyses: after one minute at 40 °C, rise at 7 °C/min to 250 °C, and hold for five minutes. At 250 °C, the injector and detector were maintained. Using a spectral range of m/z 30-440 and a solvent delay of 3.5 minutes, mass spectra were produced by electron ionization (EI) at 70 eV. Component identification was done using their mass spectra and Kovat index (KI), which were then compared to NIST and Wiley along with additional data from the literature.

2.5. Molecular docking

SARS-CoV-2 targets' X-ray crystal structure coordinates were obtained from PDB (PDB IDs: 7tjz, 6m0j, and 6vsb). Version 2.2.5 (Santa Fe, NM (USA), <http://www.eyesopen.com>) of the OpenEye scientific program was used to conduct the docking investigation. Targeted proteins' X-ray crystal structure coordinates were obtained from PDB along with their co-crystallized binding ligands. OpenEye scientific software version 2.2.5 (Santa Fe, NM (USA), <http://www.eyesopen.com>), with an academic license from The Laboratory of Yaseen A. M. Mohamed Elshaier, was used for the docking investigation. Using a virtual library of compounds, the MMFF94 force field was utilized to minimize their energies, and the OMEGA application was then used to generate multi-conformers. Omega combined the library into a single file. The OeDocking application was used to operate the generated receptor, and the target proteins were obtained from PDB. To carry out the molecular docking investigation, FRED was applied to both the ligand and the receptor input files. To forecast the ligand-receptor complex's energy profile, many scoring systems were used. The visualization technique employed was Vida.

2.6. Molecular dynamic (MD) simulations

2.6.1. Molecular dynamic simulations

Exploring the physical motion of atoms and molecules that is not easily accessible by any other means is made possible by the integration of molecular dynamic (MD) simulations in biological systems investigations [34]. The knowledge gained from running this simulation offers a detailed viewpoint on the dynamic evolution of biological systems, including molecular affiliation and conformational changes [34]. All of the systems' MD simulations were carried out using the GPU version of the PMEMD engine found in the AMBER 18 package [35]. The General Amber Force Field (GAFF) method developed by ANTECHAMBER was used to determine the partial atomic charge of every compound [36]. Within an orthorhombic box of TIP3P water molecules, each system was implicitly solved within 10 Å of any box edge by the Leap module of the AMBER 18 package. Na⁺ and Cl⁻ counterions were added to each system using the Leap module to neutralize it. Each system underwent a 2000-step initial minimization with an imposed restraint potential of 500 kcal/mol and a 1000-step full minimization with the conjugate gradient algorithm in the absence of constraints.

To guarantee that every system had the same number of atoms and volume throughout the MD simulation, each system was progressively heated over 500 ps from 0 K to 300 K. The solutes in the system were subjected to a collision frequency of 1 ps and a potential harmonic constraint of 10 kcal/mol. Every system was then heated to a constant temperature of 300K and allowed to equilibrate for 500 ps. The number of atoms and pressure in each system were kept constant for each production

simulation to model an isobaric-isothermal (NPT) ensemble. The system's pressure was then maintained at 1 bar using a Berendsen barostat [37]. Every system was MD-simulated for 20 ns. In every simulation, the hydrogen bond atoms were constrained using the SHAKE approach. Every simulation was integrated into an SPFP precision model and used a 2fs step size. The simulations employed a Langevin thermostat with a collision frequency of 1 ps, an isobaric-isothermal ensemble (NPT) with randomized seeding, a constant pressure of 1 bar, a pressure-coupling constant of 2 ps, and a temperature of 300 K.

2.6.2. Post-MD Analysis

The CPPTRAJ module of the AMBER18 suite was used to analyze the trajectories after they were saved every 1 ps from the MD simulations [38]. All graphs and visualizations were made using a data analysis program [39] and Chimera [40].

2.6.3. Thermodynamic calculation

For estimating ligand-binding affinities, the Poisson-Boltzmann, or generalized Born, and surface area continuum solvation (MM/PBSA and MM/GBSA) techniques are helpful [41-43]. Within a specified force field, the Protein-Ligand complex molecular simulations utilized by MM/GBSA and MM/PBSA provide accurate statistical-mechanical binding -free energy. The average binding free energy is over 2000 images taken from the full 200 ns trajectory. The following can be used to depict the estimation of the change in binding-free energy (ΔG) for each molecular species (complex, ligand, and receptor) [44]:

$$\Delta G_{\text{bind}} = G_{\text{complex}} - G_{\text{receptor}} - G_{\text{ligand}} \quad (1)$$

$$\Delta G_{\text{bind}} = E_{\text{gas}} + G_{\text{sol}} - TS \quad (2)$$

$$E_{\text{gas}} = E_{\text{int}} + E_{\text{vdw}} + E_{\text{ele}} \quad (3)$$

$$G_{\text{sol}} = G_{\text{GB}} + G_{\text{SA}} \quad (4)$$

$$G_{\text{SA}} = \gamma \text{SASA} \quad (5)$$

The gas-phase energy, Coulomb energy, internal energy, and van der Waals energy are represented by the terms E_{gas} , E_{int} , E_{ele} , and E_{vdw} . The FF14SB force field words were used to assess the E_{gas} . Based on the energy involvement of the polar states (GGB) and non-polar states (G), the calculation of the solution-free energy (G_{sol}) was performed. Using a water probe radius of 1.4 Å, the non-polar solvation free energy (G_{SA}) was calculated from the Solvent Accessible Surface Area (SASA) [45, 46]. On the other hand, the polar solvation (GGB) contribution was evaluated by solving the GB equation. The total entropy of the solute and temperature are represented by items S and T, respectively. The contribution of each residue to the total binding free energy was determined using Amber18's MM/GBSA-binding free energy approach.

2.7. Physicochemical and preADME parameters

Software commands were used to determine the anticipated ADMET parameters and the rule of five. The results are automatically generated. The online tool kit Mol inspiration (<https://www.molinspiration.com/>), and the free websites <https://www.molsoft.com/servers.html>, <https://preadmet.webservice.bmdrc.org/> (accessed on December 23, 2023) were used to compute Lipinski's rule (Rule of Five) and PreADME properties.

2.8. Statistical Analysis

Every experiment was carried out in three biological replications. The software titled GraphPad Prism 8.01 was used to perform statistical tests and exhibit the data graphically. The average of the means is used to display the data. The nonlinear fit of "Normalize" and "Transform" of the acquired data is represented by the IC_{50} and CC_{50} curves; their values were determined as the "best fit value" using GraphPad Prism.

2.9. Ethical Approval

The NRC ethics committee accepted the protocol, which was followed in the completion of all procedures and tests (approval number: NRC-20074).

3. Results

Clear essential oil residues with a fragrant odor were isolated through hydrodistillation of *Citrus sinensis* peels, *Artemisia cina* flowers, *Coriandrum sativum* fruits, *Lavendula officinalis* flowers, *Pimpinella anisum* fruits, *Cymbopogon citratus* aerial parts, *Rosmarinus officinalis* aerial parts, and *Thymus vulgaris* aerial parts, with yields of 0.124%, 0.151%, 0.033%, 1.122%, 0.910%, 0.185%, 0.073%, and 0.120% (w/w), respectively.

3.1. Cytotoxicity assay

Based on the experimental data, the cytotoxicity results (Fig. 2) proved that the most secure oil on MDCK cells was *A. cina* (h) oil with a CC_{50} of 1545 µg/mL, followed by *P. anisum* (d) and *C. sativum* (b) with CC_{50} s of 581.5 and 561.3 µg/mL, respectively. Conversely, the more toxic one on MDCK cells was *T. vulgaris*. In the case of VERO cells (Fig. 3), the safest oil was *C. sativum* (b) with a CC_{50} of 580.8 µg/mL, followed by *C. sinensis* (g) with a CC_{50} of 580.7 µg/mL, and *R. officinalis* (f) with a CC_{50} of 557.9 µg/mL. The safest oil assessed on VERO E6 cells against the SARS-CoV-2 virus (Fig. 4) was *C. sinensis* (g) with a CC_{50} of 216.7 µg/mL, followed by *R. officinalis* (f) and *P. anisum* (d) with CC_{50} s of 205.0 and 198.7 µg/mL, respectively. Almost all oils were safe on different cells except *C. citratus* (a), which had toxicity on MDCK cells and VERO E6 cells with CC_{50} values of 29.28 and 33.73 µg/mL, respectively.

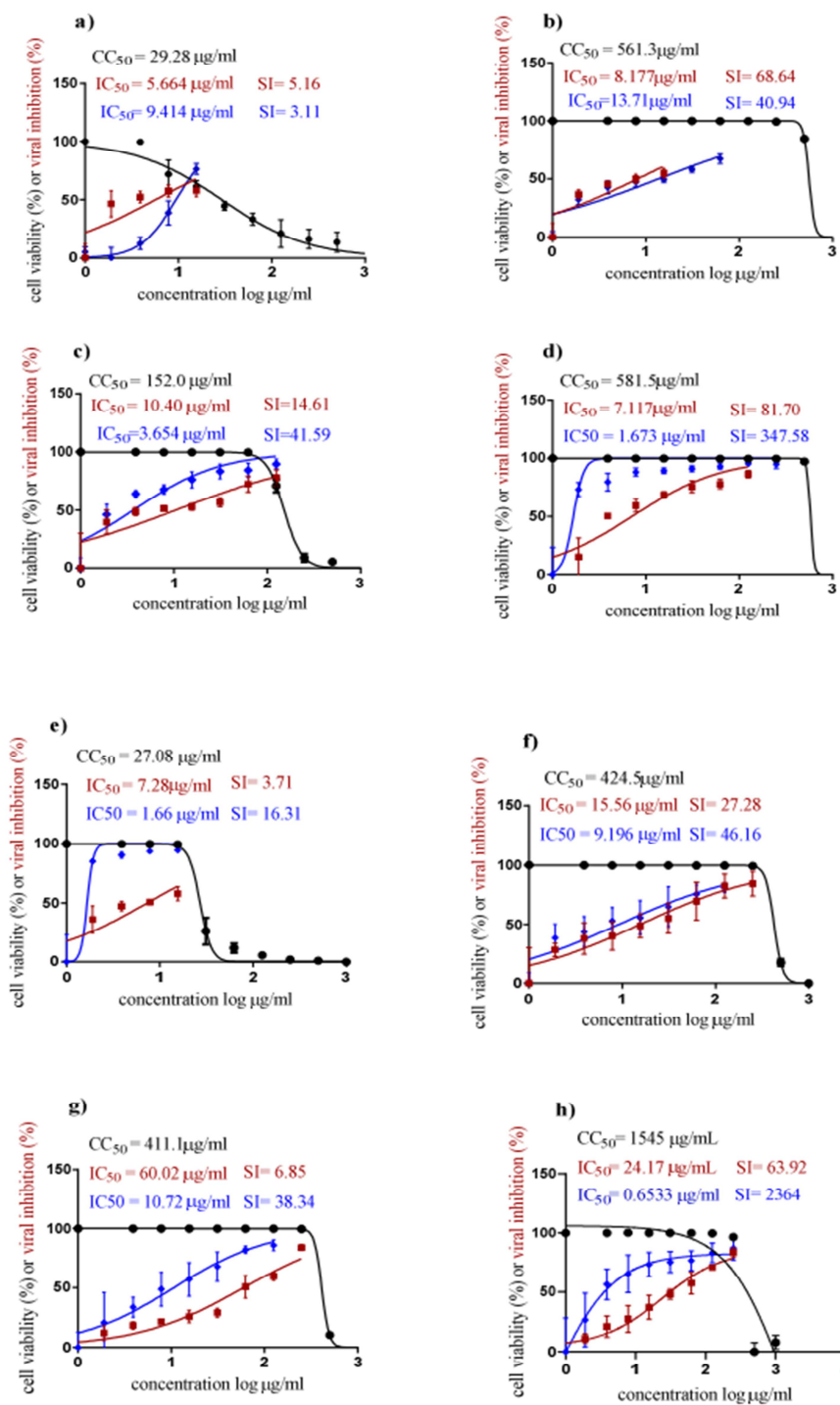


Figure 2: Cytotoxicity Concentration 50% (CC_{50}), inhibitory concentrations 50% (IC_{50}) graph against H5N1 (red color), and safety index of *C. citratus* (a), *C. sativum* (b), *L. officinalis* (c), *P. anisum* (d), *T. vulgaris* (e), *R. officinalis* (f), *C. sinensis* (g), and *A. cina* (h). Plotting log inhibitor versus normalized response (varying slope) allowed for the nonlinear regression analysis. CC_{50} and IC_{50} values were calculated using GraphPad Prism software (version 8.01).

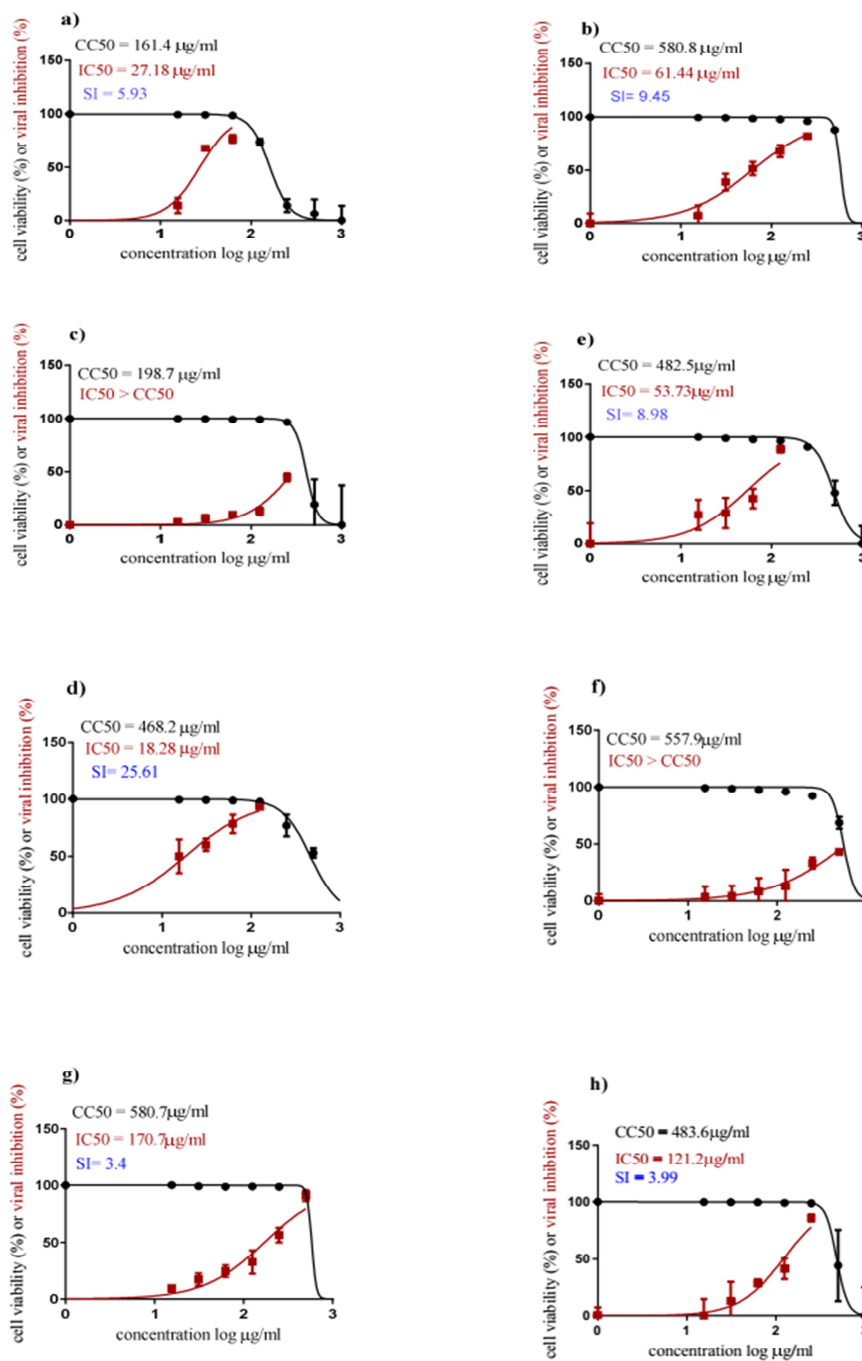


Figure 3: Cytotoxicity Concentration 50% (CC50), inhibitory concentrations 50% (IC50) graph against herpes simplex type 1 and Safety Index of *C. citratus* (a), *C. sativum* (b), *L. officinalis* (c), *P. anisum* (d), *T. vulgaris* (e), *R. officinalis* (f), *C. sinesis* (g), and *A. cina* (h). Plotting log inhibitor versus normalized response (varying slope) allowed for the nonlinear regression analysis. CC50 and IC50 values were calculated using GraphPad Prism software (version 8.01).

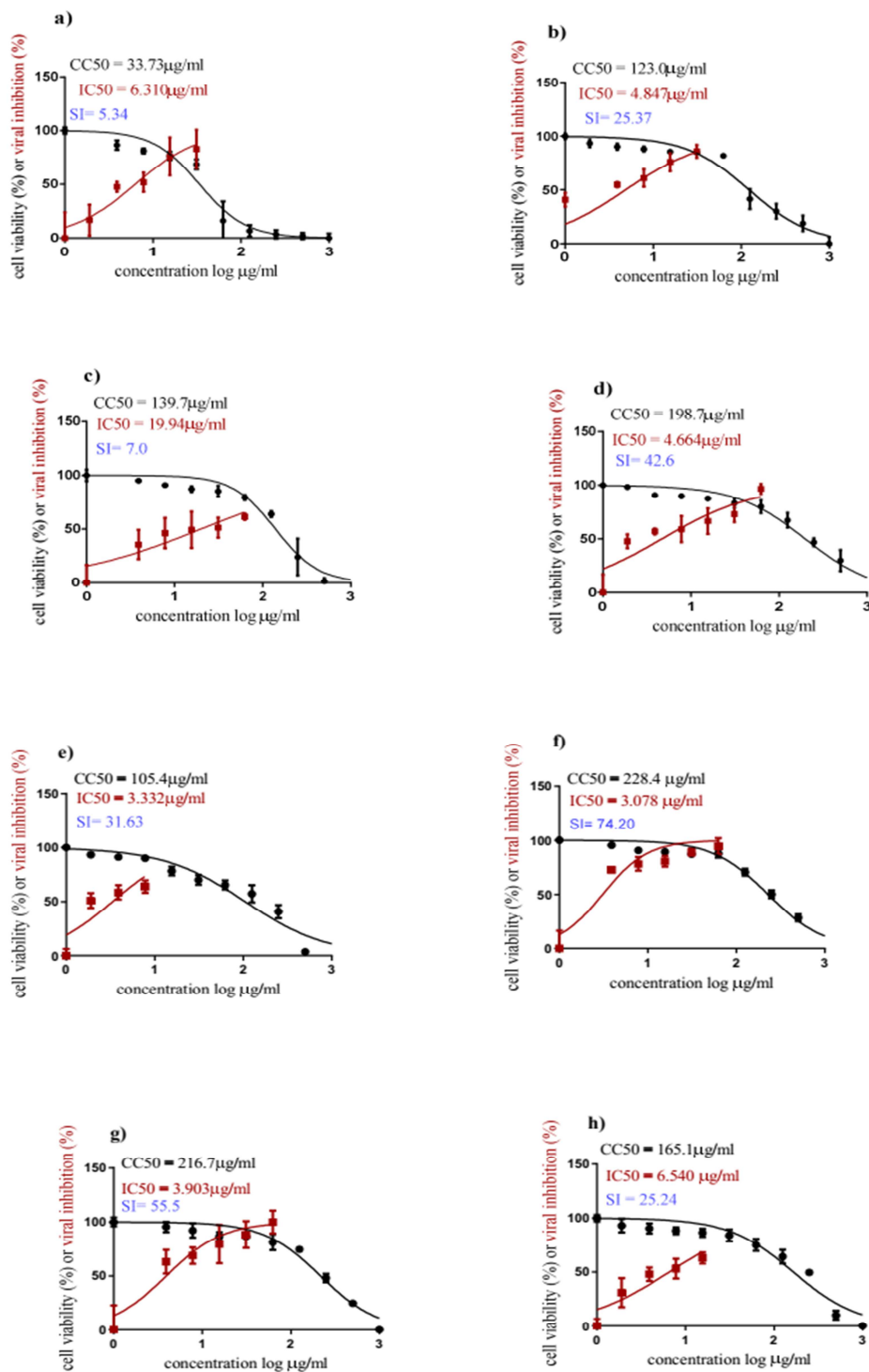


Figure 4: Cytotoxicity Concentration 50% (CC₅₀), inhibitory concentrations 50% (IC₅₀) graph showing inhibition of SARS-CoV-2 and safety index of *C. citratus* (a), *C. sativum* (b), *L. officinalis* (c), *P. anisum* (d), *T. vulgaris* (e), *R. officinalis* (f), *C. sinensis* (g), and *A. cina* (h). Plotting log inhibitor versus normalized response (varying slope) allowed for the nonlinear regression analysis. CC₅₀ and IC₅₀ values were calculated using GraphPad Prism software (version 8.01).

3.2. Antiviral activity

Inhibitory Concentration 50 (IC₅₀)

Finding the oil concentration that inhibits viral propagation by 50% requires knowledge of the inhibitory concentration (IC₅₀). The VOs of *C. sativum* (b) and *P. anisum* (d) had antiviral activity against H5N1 (Fig. 2), with inhibitory concentrations of 8.117 µg/mL and 7.117 µg/mL and a safety index equal to 68.64 and 81.7, respectively. As well, the two VOs had antiviral activity against H1N1 (Fig. 2), with inhibitory concentrations of 1.673 µg/mL of *P. anisum* (d) and 13.71 µg/mL of *C. sativum* (b). The VOs demonstrated antiviral activity against Herpes simplex type 1 (HSV-1), a DNA virus (Fig. 3), which mostly causes infections associated with or after influenza infection. The best one from the tested VOs (Fig. 2) was *P. anisum* (d), with a selectivity index (SI) of 25, inhibitory concentrations of 18.28 µg/mL, and a cytotoxic concentration value of 468.2 µg/mL on Vero cells. Almost eight VOs had antiviral activity against SARS-CoV-2 (Fig. 4), with inhibitory concentration values of 3.078 µg/mL, 3.332 µg/mL, 3.903 µg/mL, 4.664 µg/mL, 4.847 µg/mL, 6.310 µg/mL, 6.540 µg/mL, and 19.94 µg/mL of *R. officinalis* (f), *T. vulgaris* (e), *C. sinensis* (g), *P. anisum* (d), *C. sativum* (b), *C. citratus* (a), *A. cina* (h), and *L. officinalis* (c), respectively. The broad safety index (SI) of 74 for *R. officinalis* was the highest one, followed by *C. sinensis* (SI of 55) and *P. anisum* (SI of 42).

3.3. GC-MS analysis of the effective volatile oils

After screening the volatile oils of *C. citratus*, *C. sativum*, *L. officinalis*, *P. anisum*, *T. vulgaris*, *R. officinalis*, *C. sinensis*, and *A. cina* as antiviral agents against SARS-CoV-2, H5N1, H1N1, and HSV, the most potent VOs against these viruses were chosen for GC-MS examination. The VOs of *C. sativum*, *P. anisum*, and *R. officinalis* were examined using GC-MS analysis to determine the components in charge of their efficacy (see total ion chromatograms S1–S3). The composition of *C. sativum*, *P. anisum*, and *R. officinalis* VOs according to GC-MS analysis was presented in Tables 2, 3, and 4, respectively, while their chemical structures were listed in Fig. 5.

Table 2: GC-MS analysis of *C. sativum* volatile oil

Peak No.	R _t (min)	Area Sum (%)	Mol. formula	m/z	KI (obs)	KI (lit)	Identified Compounds	Class	Ref.
1	8.778	1.14	C ₁₀ H ₁₆	136	942	942	alpha-Pinene	Monoterpene hydrocarbons	[47]
2	9.206	0.11	C ₁₀ H ₁₆	136	956	955	Camphene	Monoterpene hydrocarbons	[47]
3	9.906	0.22	C ₁₀ H ₁₆	136	980	980	beta-Pinene	Monoterpene hydrocarbons	[47]
4	10.206	0.24	C ₁₀ H ₁₆	136	990	991	beta-Myrcene	Monoterpene hydrocarbons	[47]
5	11.126	0.65	C ₁₀ H ₁₆	136	1017	1019	Limonene	Monoterpene hydrocarbons	[47]
6	11.226	1.02	C ₁₀ H ₁₄	134	1016	1020	O-Cymene	Monoterpene hydrocarbons	[47]
7	11.821	2.23	C ₁₀ H ₁₆	136	1032	1035	gamma-Terpinene	Monoterpene hydrocarbons	[47]
8	12.745	0.12	C ₈ H ₁₄ O	126	1057	1059	2-Octyn-1-ol	Oxygenated monoterpene	MS
9	12.902	0.15	C ₈ H ₁₈ O	130	1065	1067	1-Octanol	Oxygenated monoterpene	MS
10	13.521	85.4	C ₁₀ H ₁₈ O	154	1080	1083	Linalool	Oxygenated monoterpene	[47]
11	14.74	1.6	C ₁₀ H ₁₆ O	152	1119	1124	Camphor	Oxygenated monoterpene	[47]
12	15.126	0.25	C ₁₀ H ₁₈ O	154	1131	1137	Terpinen-4-ol	Oxygenated monoterpene	[47]
13	15.254	0.39	C ₁₀ H ₁₈ O	154	1146	1149	endo-Borneol	Oxygenated monoterpene	[47]
14	15.578	0.26	C ₁₀ H ₁₈ O	154	1181	1185	alpha-Terpineol	Oxygenated monoterpene	[48]
15	15.645	0.31	C ₁₀ H ₂₀ O	156	1196	1201	Decanal	Oxygenated monoterpene	[48]
16	16.85	1.62	C ₁₀ H ₁₈ O	154	1250	1255	Geraniol	Oxygenated monoterpene	[48]
17	17.111	0.54	C ₉ H ₁₆ O	140	1269	1276	2-Nonenal, (E)-	Oxygenated monoterpene	[49]
18	18.973	3.64	C ₁₂ H ₂₀ O ₂	196	1366	1373	Geranyl acetate	Oxygenated monoterpene	[48]

Table 3: GC-MS analysis of *P. anisum* volatile oil

Peak No.	R _t (min)	Area Sum (%)	Mol. formula	m/z	KI (obs)	KI (lit)	Identified Compounds	Class	Ref.
1	11.125	0.06	C ₁₀ H ₁₆	136	1016	1019	Limonene	Cyclic monoterpene,	MS
2	11.225	0.12	C ₁₀ H ₁₄	134	1022	1020	<i>O</i> -Cymene	Aromatic hydrocarbon	MS
3	15.449	1.27	C ₁₀ H ₁₂ O	148	1190	1196	Estragole	Phenylpropanoid	[50]
4	17.516	88.3	C ₁₀ H ₁₂ O	148	1278	1284	Anethole	Phenylpropanoid	[50]
5	17.883	0.12	C ₁₀ H ₁₆	136	1298	1307	Cyclopentene, 4-ethenyl-1,5,5-trimethyl-	Cyclic	MS
6	19.573	0.32	C ₁₀ H ₁₂ O ₂	164	1345	1340	2-(4-methoxy-3-methylphenyl) oxirane	Phenolic	MS
7	19.959	0.21	C ₁₀ H ₁₂ O ₂	164	1377	1385	Anisketone	Phenolic	[51]
8	20.202	4.93	C ₁₅ H ₂₄	204	1398	1412	Longifolene	Tricyclic sesquiterpene	[52]
9	20.71	0.3	C ₁₅ H ₂₄	204	1290	1351	alpha-Longipinene	monoterpene	[50]
10	20.816	0.68	C ₁₅ H ₂₄	204	1420	1428	alpha-Himachalene	Sesquiterpene	[51]
11	21.035	0.43	C ₁₅ H ₂₄	204	1423	1433	alpha-Bergamotene	Sesquiterpene	[51]
12	21.092	0.18	C ₁₅ H ₂₄	204	1488	1506	beta-Bisabolene	Sesquiterpene	[50]
13	23.959	0.25	C ₂₀ H ₂₇ N O ₂	313	1569	1576	Preg-4-en-3-one, 17-alpha-hydroxy-17-beta-cyano-	Sterol derivative	MS
14	27.345	2.19	C ₁₅ H ₂₀ O ₃	248	1809	1821	Pseudoisoeugenol 2- methyl butanoate	Phenolic ester	[51]
15	28.331	0.63	C ₁₅ H ₂₀ O ₄	264	1871	1882	Thellungianin G	Phenolic ester	[51]

Table 4: GC-MS analysis of *R. officinalis* volatile oil

Peak No.	R _i (min)	Area Sum (%)	Mol. formula	m/z	KI (obs)	KI (lit)	Identified Compounds	Class	Ref.
1	8.497	0.12	C ₁₀ H ₁₆	136	926	928	Tricyclo[2.2.1.0(2.6)]heptane, 1,7,7-trimethyl-	Monoterpene hydrocarbons	[53]
2	8.783	11.51	C ₁₀ H ₁₆	136	945	942	alpha-Pinene	Monoterpene hydrocarbons	[53]
3	9.211	2.88	C ₁₀ H ₁₆	136	958	955	Camphene	Monoterpene hydrocarbons	[53]
4	9.392	0.63	C ₁₀ H ₁₄	134	964	956	Bicyclo[3.1.0]hex-2-ene, 4-methylene-1-(1-methylethyl)-	Monoterpene	[53]
5	9.911	0.31	C ₈ H ₁₆ O	128	978	976	1-Octen-3-ol	Hydrocarbon alcohol	MS
6	10.206	0.65	C ₁₀ H ₁₆	136	983	980	beta-Pinene	Monoterpene	[53]
7	10.644	0.5	C ₁₀ H ₁₆	136	997	991	beta-Myrcene	Monoterpene	[54]
8	10.735	0.32	C ₁₀ H ₁₆	136	1016	1019	Limonene	Cyclic monoterpene	[53]
9	11.13	2.89	C ₁₀ H ₁₄	134	1019	1020	O-Cymene	Monoterpene	[54]
10	11.235	1.96	C ₁₀ H ₁₈ O	154	1020	1023	Eucalyptol	Monoterpene	[53]
11	11.38	24.74	C ₁₀ H ₁₆	136	1023	1040	beta-Ocimene	Monoterpene	MS
12	12.497	0.12	C ₁₀ H ₁₆	136	1052	-	Bicyclo[4.1.0]heptane, 7-(1-methylethylidene)-	Monoterpenoids	MS
13	12.849	0.12	C ₁₀ H ₁₂	132	1060	1050	p-cymenene	Monoterpene hydrocarbon	MS
14	13.435	5.97	C ₁₀ H ₁₈ O	154	1078	1083	Linalool	Monoterpene alcohol	[54]
15	14.049	0.18	C ₁₀ H ₁₈ O	154	1094	-	2-Decyn-1-ol	Hydrocarbon alcohol	NIST
16	14.173	0.16	C ₁₀ H ₁₆ O	152	1097	1100	Camphen-6-ol	Monoterpene alcohol	MS
17	14.249	0.32	C ₁₀ H ₁₄ O	150	1099	1105	2-Pinen-7-one	Bicyclic ketone	MS
18	14.502	0.19	C ₁₀ H ₁₆ O	152	1106	1106	cis-Verbenol	Bicyclic monoterpene alcohols.	[54]
19	14.745	22.24	C ₁₀ H ₁₆ O	152	1113	1123	Camphor	Monoterpene ketone	[54]
20	14.992	1.39	C ₁₀ H ₁₈ O	154	1129	1137	Terpinen-4-ol	Monoterpene alcohol	[54]
21	15.054	11.44	C ₁₀ H ₁₈ O	154	1146	1149	endo-Borneol	Bicyclic monoterpene	[54]
22	15.13	0.22	C ₁₀ H ₁₆ O	152	1150	1159	3-Pinanone	Bicyclic monoterpene	MS
23	15.264	1.16	C ₁₀ H ₁₄ O	150	1154	1162	Pinocarvone	Bicyclic monoterpene	[54]
24	15.583	1.85	C ₁₀ H ₁₈ O	154	1180	1185	alpha-Terpineol	Monoterpene alcohol	[54]
25	15.878	0.29	C ₁₀ H ₁₆ O	152	1143	1194	Myrtenol	Monoterpene alcohol	[55]
26	16.011	0.66	C ₁₁ H ₁₈ O	166	1207	1212	Nopol	Bicyclic monoterpene	MS
27	16.559	4.07	C ₁₀ H ₁₄ O	150	1210	1217	Verbenone	Monoterpene ketone	[54, 56]
28	16.754	0.47	C ₁₀ H ₁₆	136	1219	-	7-isopropylidene-bicyclo[4.1.0]heptane	Monoterpene	MS
29	16.897	0.94	C ₁₀ H ₁₈ O	154	1230	1234	(-)-cis-Myrtanol	Monoterpene alcohol	MS
30	17.297	0.46	C ₁₂ H ₂₀ O ₂	196	1275	1281	Bornyl acetate	Monoterpene	[54]
31	17.388	0.3	C ₁₀ H ₁₂ O	148	1279	1284	Anethole	Monomethoxyb enzene	MS
32	19.05	0.16	C ₁₁ H ₁₈	150	1280	-	Bicyclo[5.1.0]octane, 8-(1-methylethylidene)-	Bicyclic monoterpene	MS
33	19.535	0.22	C ₁₀ H ₁₀ O ₂	162	1378	1388	2-Propenoic acid, 3-phenyl-, methyl ester	Cinnamic ester	MS
34	19.716	0.31	C ₁₅ H ₂₄	204	1411	1418	Caryophyllene	Sesquiterpene	[54]
35	20.578	0.25	C ₁₅ H ₂₆ O	222	1544	1554	Nerolidol	Acyclic Sesquiterpene	MS

MS, NIST, and Wiley library

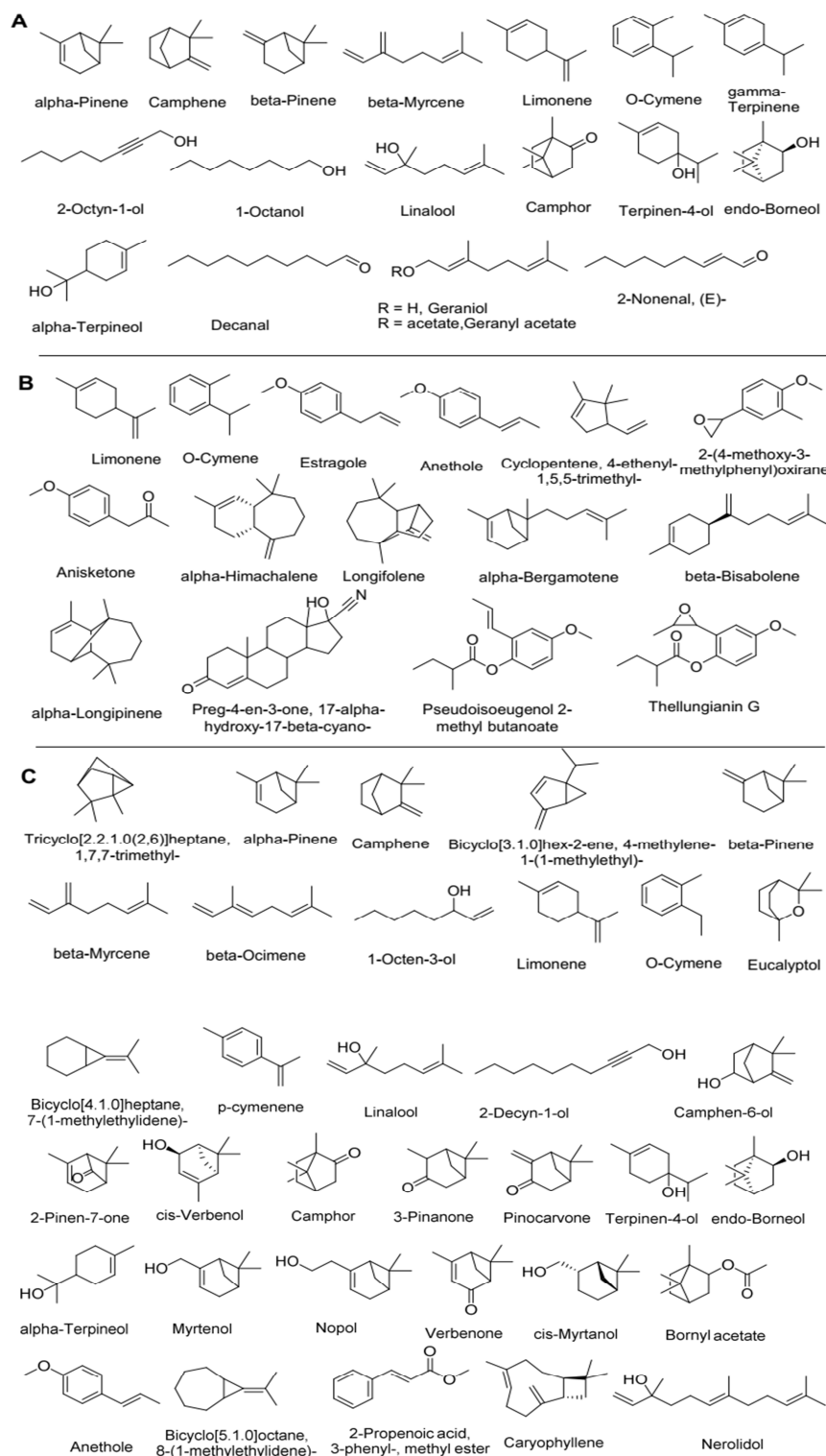


Figure 5: Chemical structure of the identified compounds using GC-MS analysis: A: *C. sativum* volatile oil, B: *P. anisum* volatile oil, and C: *R. officinalis* volatile oil.

3.4. Antiviral enzymatic assays against SARS-CoV-2

To explore the possible mechanism of action, the most potent anti-SARS-CoV-2 VO (*R. officinalis*) and the most effective antiviral VO tested against all viral strains (*P. anisum*) along with anethole, the major compound in *P. anisum* VO, were selected.

3.4.1. ACE2 Enzyme Inhibitory Activity

The *in vitro* ACE2 enzyme inhibitory activity of *P. anisum* and *R. officinalis* (both at 5 mg/mL concentration) along with anethole (at 5 mg/mL concentration) was assessed. The results presented in Table 5 showed that *P. anisum* VO had a higher ACE2 inhibitory activity compared to *R. officinalis* VO, anethole, remdesivir, and molniravir, but was less potent than hydroxychloroquine.

3.4.2. Spike Protein RBD Enzyme Inhibitory Activity

P. anisum VO showed 76% spike protein RBD enzyme inhibitory activity, which was the highest percent compared to other VOs or the standard antiviral drugs (Table 5). The inhibitory activity percentage was reduced from 76% to 61%, 48%, and 46% for remdesivir, molniravir, and *R. officinalis* VO, respectively.

3.4.3. PLpro Enzyme Inhibitory Activity

Compared to the standard antiviral drugs (Table 5), *P. anisum* VO was the most potent sample, with a percent up to 76.8% effective against papain-like protease enzyme.

Table 5: Percent inhibition of the most active antiviral VOs along with anethole, the major VO component in *P. anisum*

V.O/compound	Conc.	Mean % inhibition \pm SD		
		Spike protein RBD	PLpro	ACE2
<i>R. officinalis</i>	5 mg/mL	46.00 \pm 2.8284	44.32 \pm 1.3790	20.83 \pm 1.3598
<i>P. anisum</i>	5 mg/mL	76.00 \pm 5.6568	76.80 \pm 1.1618	39.42 \pm 3.1729
Anethole	5 mg/mL	33.50 \pm 1.1048	22.33 \pm 1.5310	12.50 \pm 2.2663
Hydroxychloroquine	5 mg/mL	27.37 \pm 1.9940	83.80 \pm 3.5355	69.00 \pm 5.6568
Remdesivir	500 μ g/mL	61.47 \pm 1.2244	88.67 \pm 1.3773	7.14 \pm 2.6799
Molniravir	500 μ g/mL	48.05 \pm 1.8366	89.84 \pm 1.2803	16.32 \pm 0.8246

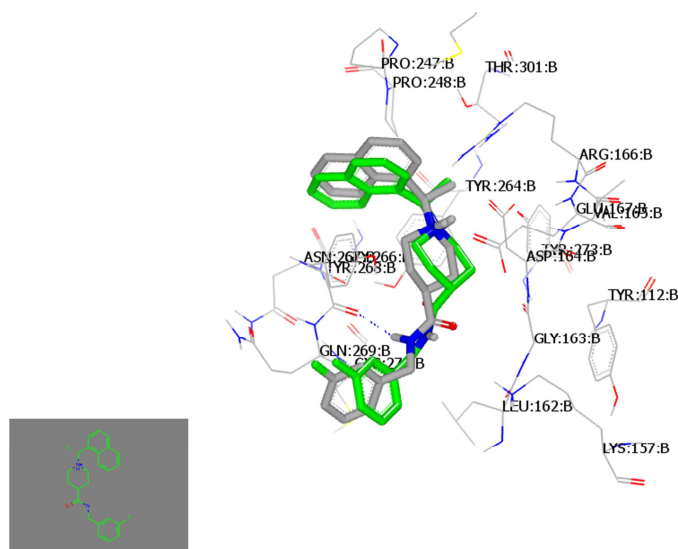
3.5. Molecular Docking Study

After selecting VOs *C. sativum*, *P. anisum*, and *R. officinalis* depending on their activity against tested viral strains to be analyzed through the GC-MS technique, the major components in each VO were examined in the molecular docking study. Anethole, longifolene (from *P. anisum*), α -pinene, camphor, endoborneol, eucalyptol (from *R. officinalis*), and linalool (from *C. sativum*) were examined in this docking study.

3.5.1. Molecular docking study with SARS-CoV-2 papain-like protease (PDB:ID 7T2J) [57]

To validate our docking study, the co-crystallized ligand (N-[(3-fluorophenyl)methyl]-1-[(1R)-1-naphthalen-1-ylethyl]piperidine-4-carboxamide-S88) was redocked with the downloaded protein and created receptor by OpenEye software. Both structures are overlaid with each other completely (Fig. 6a). In (Fig. 6b), anethole docked with the receptor in the same pocket as the co-crystallized ligand. Moreover, all volatile oils with a high ratio, namely linalool, anethole, longifolene, α -pinene, camphor, endoborneol, and eucalyptol, were clustered in the same cleft (Fig. 6c). Compound consensus scores are represented in Table 6.

a)



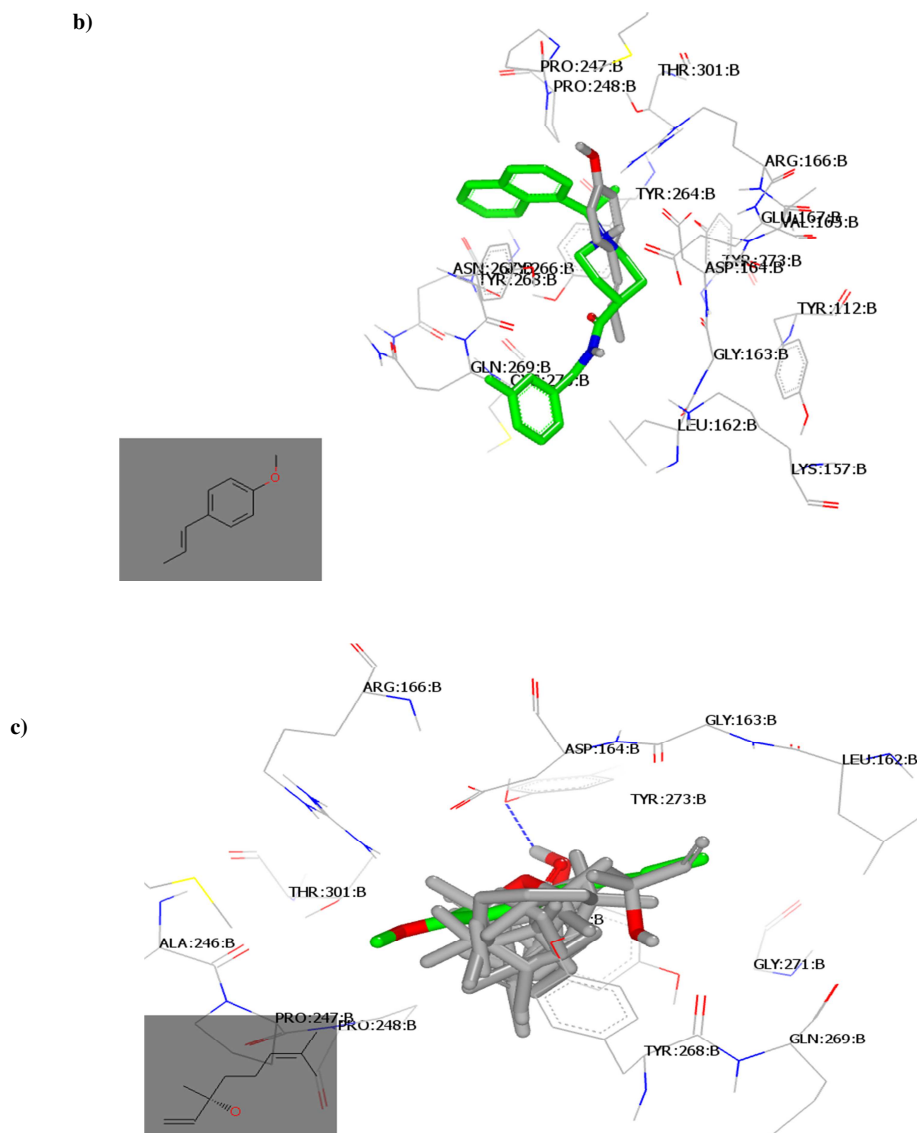


Figure 6: Visual representation by the Vida application for the docking of selected compounds with SARS-CoV-2 papain-like protease (PDB:ID 7TZJ): (a) standard ligand redocked; (b) anethole (green color) with the standard co-crystallized ligand (grey); (c) selected VO's major compounds clustered in the same domain in the receptors.

Table 6: Compound consensus scores for selected VO's major compounds with PDB:ID 7TZJ

Compound	Consensus Score	Binding interaction
S88	3.0000	HB with Gln:269A
Linalool	32.0000	Hydrophobic-hydrophobic
Anethole	33.0000	Hydrophobic-hydrophobic
Longifolene	39.0000	Hydrophobic-hydrophobic
α -Pinene	41.0000	Hydrophobic-hydrophobic
Camphor	46.0000	Hydrophobic-hydrophobic
Endoborneol	47.0000	HB with Tyr:273A
Eucalyptol	51.0000	Hydrophobic-hydrophobic

3.5.2. Docking with the SARS-CoV-2 spike receptor-binding domain bound with ACE2 (PDB:ID 6M0J) [58]

In (Fig. 7a), anethole docked with the receptor in a hydrophobic-hydrophobic interaction. Moreover, all volatile oils with a high ratio, namely linalool, anethole, longifolene, α -pinene, camphor, endoborneol, and eucalyptol were clustered in the same cleft (Fig. 7b). The compound consensus score is represented in Table 7.

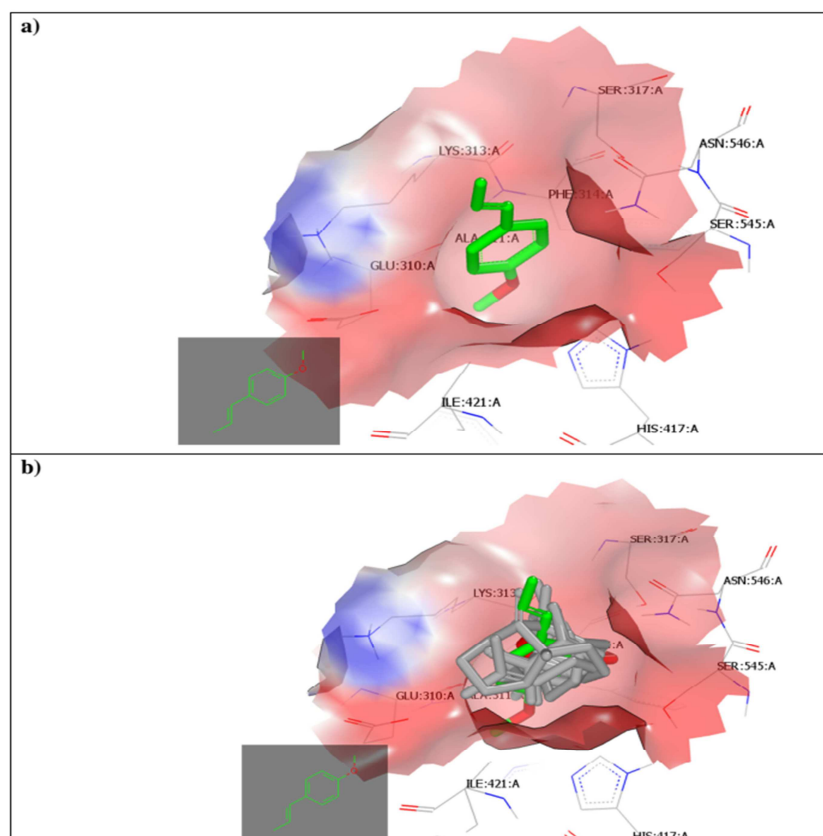


Figure 7: Visual representation by the Vida application for the docking of selected compounds with the SARS-CoV-2 spike receptor-binding domain bound with ACE2 (PDB:ID 6M0J): (a) anethole; (b) selected VO's major compounds clustered in the same domain in the receptors.

Table 7: Compound consensus scores for selected VO's major compounds with PDB:ID 6M0J

Compound	Consensus Score	Binding interaction
2-acetamido-2-deoxy-beta-D-glucopyranose	5.0000	Hydrophobic-hydrophobic
α - Pinene	32.0000	Hydrophobic-hydrophobic
Endoborneol	35.0000	Hydrophobic-hydrophobic
Linalool	39.0000	Hydrophobic-hydrophobic
Camphor	41.0000	Hydrophobic-hydrophobic
Longifolene	46.0000	Hydrophobic-hydrophobic
Anethole	49.0000	Hydrophobic-hydrophobic
Eucalyptol	50.0000	Hydrophobic-hydrophobic

3.5.3. Docking with SARS-CoV-2 spike receptor (PDB:ID 6VSB) [59]

The compound pattern was changed in the case of interaction with the spike glycoprotein. Anethole docked with the receptor in a hydrophobic hydrophobic interaction (Fig. 8a), and other VO's major components were clustered outside the receptor, except anethole and linalool which were overlaid and interacted with the same domains inside the receptor (Fig. 8b). Compound consensus scores are represented in Table 8.

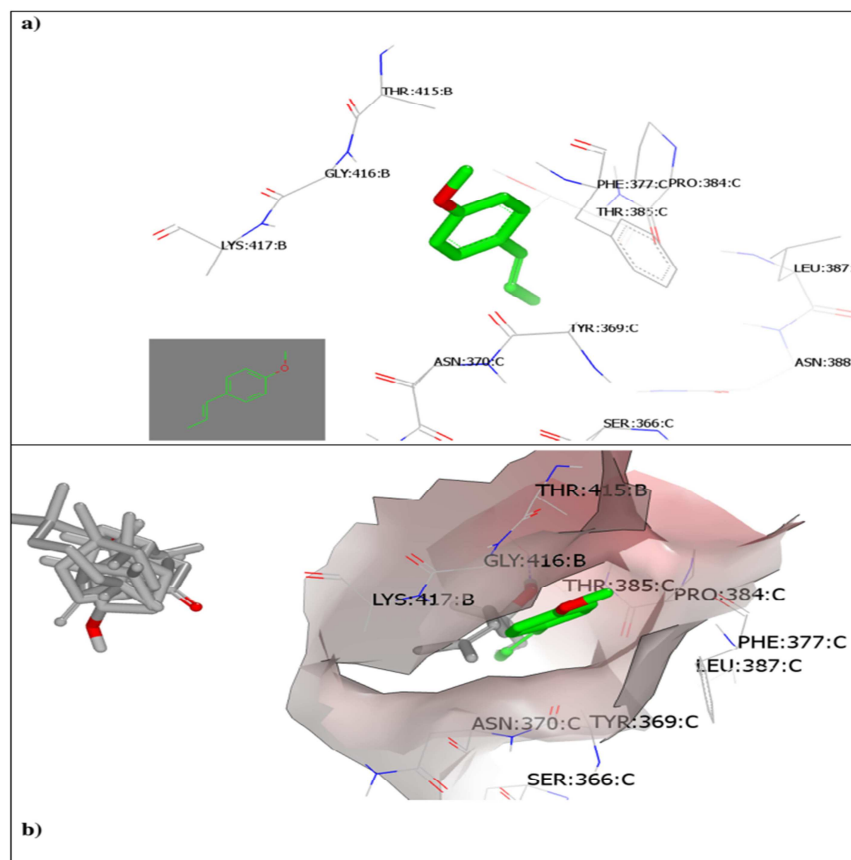


Figure 8: Visual representation by the Vida application for the docking of selected compounds with the SARS-CoV-2 spike receptor (PDB:ID 6VSB): (a) anethole; (b) selected VO's major compounds clustered outside the receptor except anethole and linalool.

Table 8: Compound consensus scores for selected VO's major compounds with PDB:ID 6VSB

compound	Consensus Score
S88	12.0000
Longifolene	35.0000
α -Pinene	42.0000
Linalool	42.0000
Camphor	48.0000
Anethole	49.0000
Endoborneol	54.0000
Eucalyptol	54.0000

3.6. Predicted ADMET calculations

It states that for a substance to be a promising biologically active molecule, it must meet the following criteria: (1) molecular weight <500, (2) log P (lipophilicity) <5, (3) < 5 H-bond donors (sum of NH and OH), (4) <10 H-bond acceptors (sum of N and O), and (5) <10 rotatable bonds (an additional criterion provided by Veber) and also should show no more than one violation of the above criteria. On the basis of the above criteria, the extracted compounds were subjected to *in silico* tests for ADMET prediction for testing the bioavailability, toxicity, Lipinski's rule of five, topological polar surface area, and number of rotatable bonds. These calculated parameters are presented in Table 9.

According to Table 10, endoborneol, eucalyptol, and linalool illustrate the same molecular formula (154.14). Endoborneol and linalool showed the same HBD (hydrogen bond donor), HBA (hydrogen bond acceptor), and BBB (blood-brain barrier) and

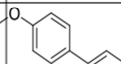
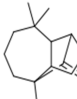
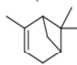
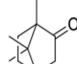
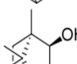
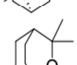
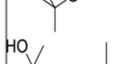
differed in the drug-likeness score. Camphor has the best drug-likeness score (0.11) with a high polar surface area (MolPSA) and low lipophilicity parameter (logP). Anethole represented the highest blood-brain barrier score (4.36); however, it has a low drug likeness score (-1.68). Anethole has the lowest value of plasma protein binding, and all compounds have 100% HIA (percentage of human intestinal absorption). For toxicity prediction by calculation of Amestest and Carcino_Mouse, all compounds showed mutagen and negative values except Eucalyptol, which illustrated mutagen and positive values, respectively.

Table 9: Topological polar surface area, number of rotatable bonds, and calculated Lipinski's rule of five for the extracted compounds using Molinspiration server

Comp.	miLog P ^a	TPSA ^b (Å ²)	MW ^c	nON ^d	nOHNH ^e	Nvoilation ^f	Nrot ^g	Vol
Anethole	3.10	9.23	148.21	1	0	0	2	153.57
longifolene	4.95	0.00	204.36	0	0	0	0	225.02
α-Pinene	3.54	0.00	136.24	0	0	0	0	151.81
Camphor	2.16	17.07	152.24	1	0	0	0	159.86
Endoborneol	2.35	20.23	154.25	1	1	0	0	165.72
Eucalyptol	2.72	9.23	154.25	1	0	0	0	166.66
Linalool	3.21	20.23	154.25	1	1	0	4	175.59

^amiLog P (the calculated n-octanol-water partition coefficient); ^bTopological polar surface area (TPSA); ^cMolecular weight (MW); ^dNumber of hydrogen bond acceptor (nON); ^eNumber of hydrogen bond donor (nOHNH); ^fNumber of violations (nvoilations); ^gNumber of rotatable bonds (nrot).

Table 10: Pre-predicted Lipinski's Rule of Five and preADME parameters of the most active compounds.

compound	Chemical structure	Lipinski's Rule of Five ^[49]					Pre-ADMET prediction ^[50]							Toxicity	
		Molecular weight	HBA	HBD	MolLog P	MolPS A	BBB Score	Drug-likeness model score	CaCo2	Skin permeability	HIA	Plasma protein binding			
													Amestest	Carcinogenicity_Mouse	
Anethole		148.09	1	0	3.27	7.78 A2	4.36	-1.68	58.08	-1.15	100.00	89.23	mutagen	negative	
longifolene		204.19	0	0	4.25	0.00 A2	1.26	-1.16	23.49	-1.17	100.00	92.35	mutagen	negative	
α-Pinene		136.13	0	0	4.49	0.00 A2	0.98	-1.45	23.63	-1.44	100.00	100.00	mutagen	negative	
Camphor		152.12	1	0	2.34	14.33 A2	4.30	0.11	26.81	-1.84	100.00	100.00	mutagen	negative	
Endoborneol		154.14	1	1	3.00	16.70 A2	4.26	-0.51	24.23	-1.88	100.00	100.00	mutagen	negative	
Eucalyptol		154.14	1	0	2.61	6.37 A2	3.88	-1.04	21.89	-1.32	100.00	100.00	mutagen	positive	
Linalool		154.14	1	1	3.07	16.84 A2	4.26	-0.99	29.35	-0.89	100.00	100.00	mutagen	negative	

HBD (hydrogen bond donor); HBA (hydrogen bond acceptor); BBB (blood-brain barrier); PPB (plasma protein binding); HIA (percentage human intestinal absorption); permeability to Caco-2 (human colorectal carcinoma) cells *in vitro*; the Ames test, a two-year mouse carcinogenicity bioassay, is a straightforward technique for determining a compound's mutagenicity [62].

3.7. Molecular dynamics and system stability

To forecast the behavior of the isolated compounds upon binding to the protein's active site as well as their interaction and stability through simulation, a molecular dynamic simulation was run [63, 64]. To identify interrupted motions and prevent any artifacts during the simulation, system stability must be validated. The stability of the systems was evaluated in this study using Root-Mean-Square Deviation (RMSD) during the 20 ns simulations. For the complete frames of the systems, the obtained average RMSD values were 3.04 ± 0.54 Å and 1.30 ± 0.13 Å for the apo and anethole-SARS-CoV-2 spike-complex,

respectively, Fig. 9A, and 1.34 ± 0.19 Å and 1.23 ± 0.17 Å for the Apo and anethole-CoV spike (S) glycoprotein, respectively. Fig. 10a, and 2.20 ± 0.36 Å, and 1.92 ± 0.40 Å, for Apo, anethole-SARS CoV-2 papain-like protease (PLpro), respectively, Fig. 11a'. These findings demonstrated that, in comparison to the other systems under investigation, the anethole-bound protein complex system developed a comparatively more stable shape.

In MD modeling, evaluating the structural flexibility of proteins following ligand binding is essential for investigating residue behavior and its relationship to the ligand [65]. The Root-Mean-Square Fluctuation (RMSF) technique was utilized to assess protein residue changes to assess the impact of inhibitor binding to the corresponding targets over 20 ns simulations. As shown in Fig. 9B, the estimated average RMSF values for the apo and anethole-SARS-CoV-2 spike complex were 1.62 ± 0.59 Å and 1.27 ± 0.55 Å, respectively, and 4.81 ± 0.60 Å, and 3.99 ± 0.40 Å, for the Apo, anethole-CoV spike (S) glycoprotein, respectively. Fig. 10b and Fig. 11b' showed 1.42 ± 0.41 Å, and 1.49 ± 0.63 Å, for Apo, anethole-SARS CoV-2 papain-like protease (PLpro), respectively. These results showed that, in comparison to the other systems, the anethole-bound-to protein complex system has less residue fluctuation.

In MD simulation, ROG was found to assess both the overall compactness of the system and its stability upon ligand binding [66, 67]. The average Rg values were 31.39 ± 0.31 Å, and 30.85 ± 0.15 Å, for the apo and anethole-SARS-CoV-2 spike complex, Fig. 9C, and 46.79 ± 0.41 Å, and 45.39 ± 0.54 Å, for the Apo and anethole-CoV spike (S) glycoprotein, respectively. Fig. 10c and Fig. 11c' showed 23.06 ± 0.12 Å, and 22.90 ± 0.16 Å, for Apo, anethole-SARS CoV-2 papain-like protease (PLpro), respectively. The behavior observed suggests that anethole-complex complexes have a very stiff structure when compared to the receptors under study. By determining the protein's solvent-accessible surface area (SASA), the compactness of the hydrophobic core of the protein was investigated. This was accomplished by measuring the protein's solvent-visible surface area, which is crucial for the stability of biomolecules [68]. The average SASA values were 34351.54 Å², and 33982 Å², for the apo and anethole-SARS-CoV-2 spike complex (Fig. 9D), and 50836.45 Å², and 50523.21 Å², for the apo and anethole-CoV spike (S) glycoprotein, respectively. Fig. 10d and Fig. 11d' showed 14580.08 Å², and 14247.00 Å², for apo, anethole-SARS-CoV-2 papain-like protease (PLpro), respectively. The anethole-complex system is still present inside the catalytic domain binding region of the receptors under study, as demonstrated by the SASA result in conjunction with the results from the RMSD, RMSF, and ROG computations.

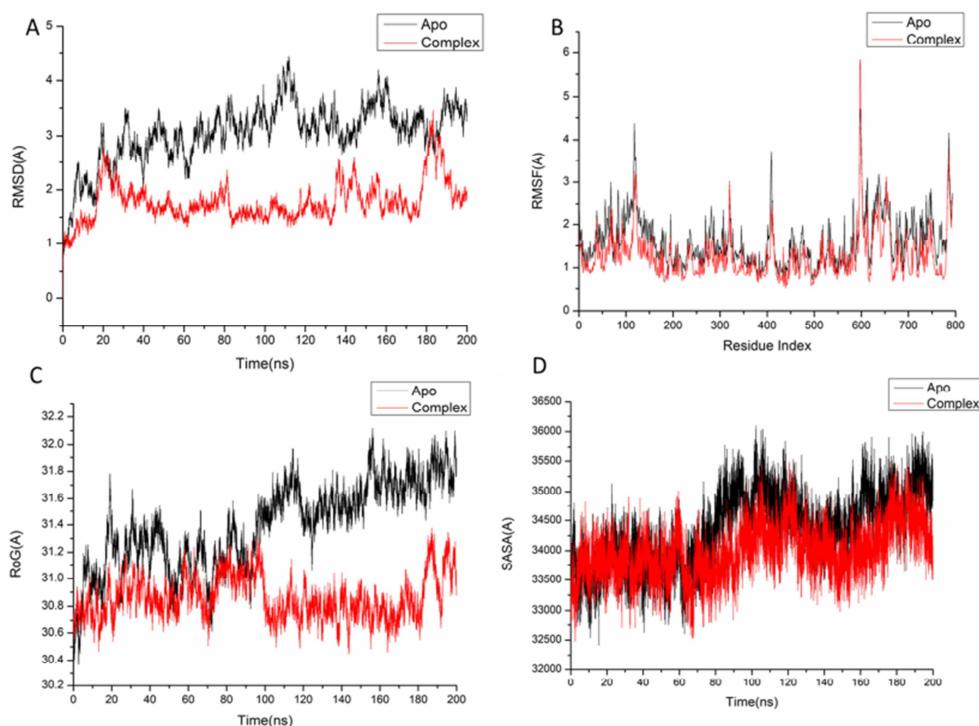


Figure 9: (A) RMSD of the protein backbone atoms' Ca atoms; (B) RMSF of each residue of the protein backbone Ca atoms of protein residues; (C) ROG of Ca atoms of protein residues; (D) Solvent accessible surface area (SASA) of the Ca of the backbone atoms relative (black) to the starting minimized over 200 ns for the ATP binding site of SARS-CoV-2 spike receptor with anethol (red).

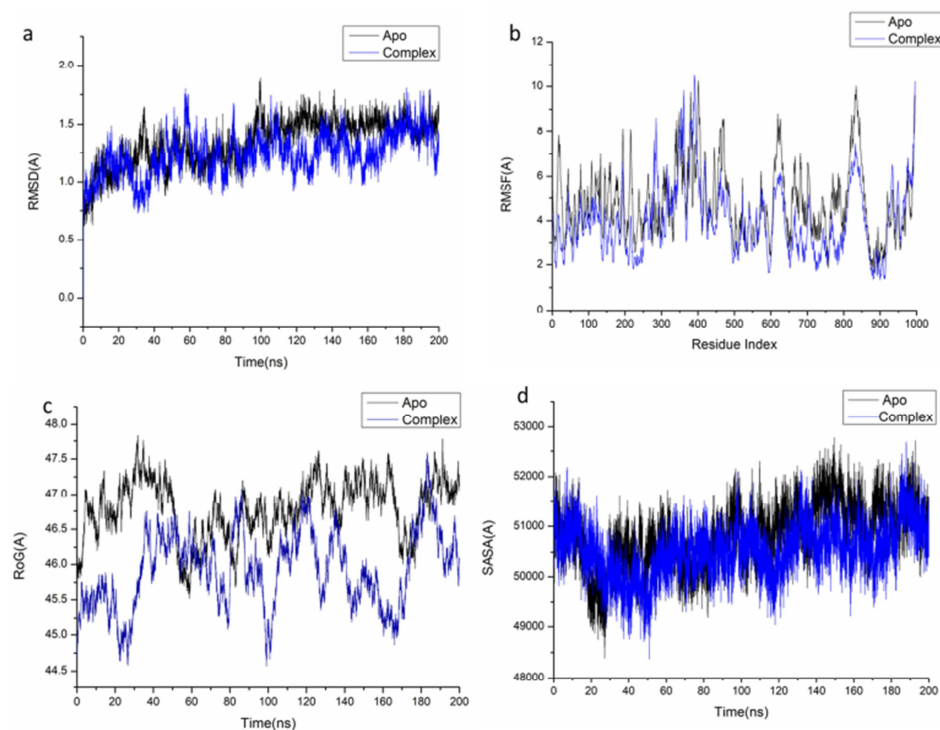


Figure 10: (a) RMSD of the protein backbone atoms' $C\alpha$ atoms; (b) RMSF of each residue of the protein backbone $C\alpha$ atoms of protein residues; (c) ROG of $C\alpha$ atoms of protein residues; (d) solvent accessible surface area (SASA) of the $C\alpha$ of the backbone atoms relative (black) to the starting minimized over 200 ns for the ATP binding site of CoV spike (S) glycoprotein receptor with anethol (blue).

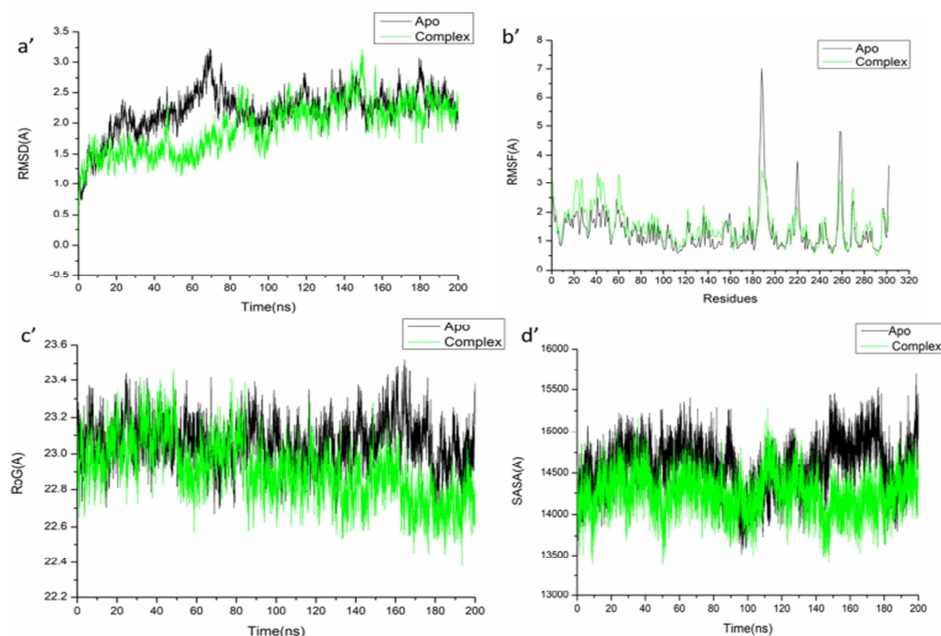


Figure 11: (a') RMSD of $C\alpha$ atoms of the protein backbone atoms. (b') RMSF of each residue of the protein backbone $C\alpha$ atoms of protein residues (c') ROG of $C\alpha$ atoms of protein residues; (d') solvent accessible surface area (SASA) of the $C\alpha$ of the backbone atoms relative (black) to the starting minimized over 200 ns for the ATP binding site of SARS CoV-2 papain-like protease (PLpro) receptor with anethol (green).

3.7.1. Binding interaction mechanism based on binding free energy calculation:

The molecular mechanics energy technique (MM/GBSA), which combines generalized Born and surface area continuum solvation, is a prominent method for measuring the free binding energies of small molecules to biological macromolecules and may be more reliable than docking scores [69]. By taking snapshots of the systems' trajectories, the binding free energies were determined using AMBER18's MM-GBSA program. Table 11 demonstrates that, with the exception of ΔG_{solv} , all reported computed energy components produced substantial negative values, indicating favorable interactions. According to the data, anethole-SARS-CoV-2 spike, anethole-CoV spike (S) glycoprotein, and anethole-SARS-CoV-2 papain-like protease systems had binding affinities of -21.43 kcal/mol, -21.83 kcal/mol, and -11.15 kcal/mol, respectively.

Table 11: The calculated energy binding for anethole compounds against the TMK receptor and CDK receptor, respectively

Energy Components (kcal/mol)					
Complex	ΔE_{vdW}	ΔE_{elec}	ΔG_{gas}	ΔG_{solv}	ΔG_{bind}
SARS-CoV-2 spike					
Anethole-complex	-24.93 \pm 0.28	-5.26 \pm 0.29	-30.55 \pm 0.44	9.21 \pm 0.29	-21.43 \pm 0.36
CoV spike (S) glycoprotein					
Anethole-complex	-25.57 \pm 0.47	-3.91 \pm 0.50	-29.48 \pm 0.42	7.64 \pm 0.21	-21.83 \pm 0.43
SARS-CoV-2 papain-like protease (PLpro) receptor					
Anethole-complex	-15.44 \pm 0.27	-2.70 \pm 0.30	-18.14 \pm 0.42	6.99 \pm 0.31	-11.15 \pm 0.26

ΔE_{elec} = electrostatic energy; ΔG_{bind} = calculated total binding free energy; ΔG_{solv} = solvation free energy; ΔE_{vdW} = van der Waals energy

The interactions between anethole and the SARS-CoV-2 spike, CoV spike (S) glycoprotein, and SARS-CoV-2 papain-like protease are fueled by the more positive Vander Waals energy and electrostatic energy components, respectively; according to a thorough analysis of each energy contribution that yields the reported binding free energies (Table 11).

3.7.2. Identification of the critical residues responsible for ligand binding:

In order to get additional insight into the significance of specific residues involved in the inhibition of the ATP binding site of the SARS-CoV-2 spike receptor, the total energy involved in the binding of these enzymes by the anethole molecule was further broken down into their individual site residue participation. As shown in Fig. 12A, residues Asn 72 (-0.67 kcal/mol), Leu 73 (-0.83 kcal/mol), Thr 74 (-0.338 kcal/mol), Lys 76 (-0.203 kcal/mol), Leu 77 (-1.991 kcal/mol), Gln 80 (-0.216 kcal/mol), Glu 190 (-0.165 kcal/mol), Val 191 (-2.396 kcal/mol), Asn 192 (-0.818 kcal/mol), Val 194 (-0.786 kcal/mol), Glu 546 (-0.365 kcal/mol), Pro 547 (-1.19 kcal/mol), and Trp 548 (-0.43 kcal/mol) are the main positive contributions of the anethole compound to the ATP binding site receptor.

However, the major favourable role of the anethole compound to the ATP binding site receptor of the CoV spike (S) glycoprotein receptor is mostly seen in the remnants Val 48 (-0.393 kcal/mol), Ile 70 (-1.55 kcal/mol), Leu 75 (-0.808 kcal/mol), Asp 76 (-0.127 kcal/mol), Leu 83 (-0.516 kcal/mol), Phe 98 (-1.312 kcal/mol), Phe100 (-1.887 kcal/mol), Cys 101 (-0.994 kcal/mol), Pro 104 (-0.418 kcal/mol), Val 113 (-0.154 kcal/mol), Tyr 114 (-0.175 kcal/mol), Ser 115 (-0.719 kcal/mol), Met 63 (-0.4 kcal/mol), Fig. 12B. Furthermore, Leu 160 (-0.932 kcal/mol), Gly 161 (-0.243 kcal/mol), Asp 162 (-0.148 kcal/mol), Pro 237 (-0.439 kcal/mol), Pro 238 (-0.673 kcal/mol), Tyr 254 (-0.707 kcal/mol), Asn 257 (-0.149 kcal/mol), Tyr 258 (-1.26 kcal/mol), Tyr 263 (-0.211 kcal/mol), and Thr 291 (-0.114 kcal/mol) residues, Fig. 12C, composed the majority of the anethole compound's favourable contribution to the ATP binding site receptor of the SARS CoV-2 papain-like protease (PLpro) receptor.

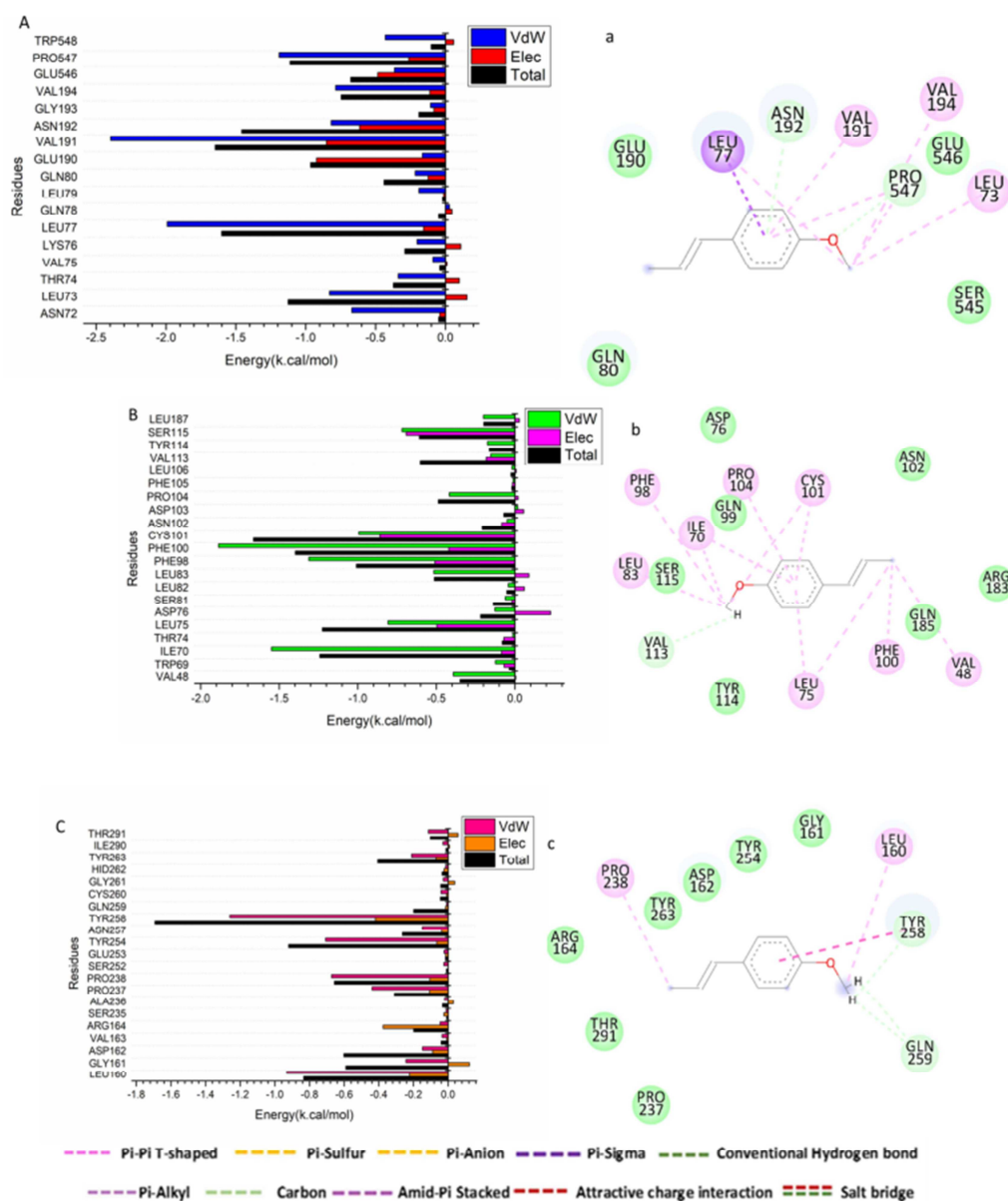


Figure 12: Per-residue breakdown plots showing the energy contributions to the binding and stabilization of anethole to the ATP binding site of the SARS-CoV-2 spike receptor (A), CoV spike (S) glycoprotein (B), and SARS-CoV-2 papain-like protease (PLpro) receptors (C).

3.7.3. Ligand-residue interaction network profiles

Making structural modifications to medicinal compounds to boost bioavailability, lower toxicity, and enhance pharmacokinetics is one goal of drug design [70]. S1 and S2 are the two subunits that make up the spike (S) protein of SARS-CoV-2, which is essential for receptor recognition and cell membrane fusion. The S2 subunit mediates viral cell membrane fusion by forming a six-helical bundle via the two-heptad repeat domain, making it a possible target for medication. The S1 subunit has a receptor-binding domain that identifies and binds to the host receptor, angiotensin-converting enzyme 2 [71]. Fig. 13A depicts an anethole compound fitting in the catalytic working site of the SARS-CoV-2 spike. Anethole compound has been discovered to create a Pi-alkyl contact with Leu 73, Val 191, and Val 194. With the phenyl and methoxy groups, the pharmacophoric hotspot residue Leu 77 has generated Pi-sigma and Pi-alkyl interactions. Conversely, a Pi-alkyl interaction

has been generated by the docked anethole-CoV spike (S) glycoprotein with Val 48, Ile 70, Leu 75, Leu 83, Phe 98, Phe 100, Cys 101, and Pro 104 (Fig. 13B). Additionally, the docked anethole-SARS-CoV-2 papain-like protease (PLpro) displays that lipophilic components account for most of the binding affinity as a result of the benzene ring forming a pi-alkyl interaction with Ile 70, Leu 75, Cys 101, and Pro 104 (Fig. 13C).

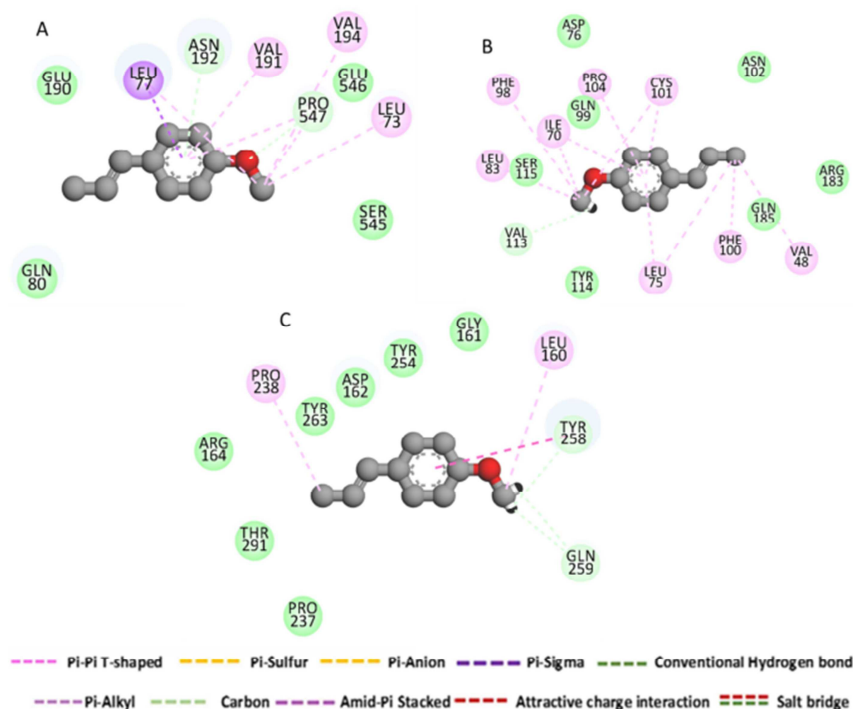


Figure 13: The interaction residue of anethole into the catalytic spot of the SARS-CoV-2 spike receptor (A), CoV spike (S) glycoprotein (B), and SARS-CoV-2 papain-like protease (PLpro) receptors (C).

4. Discussion

The emergence of drug-resistant viral strains has recently become a notable concern due to the ongoing evolution of respiratory tract viruses in their natural or intermediate reservoirs and/or the ongoing release of antiviral drugs into the environment as a result of unrestricted drug prescription to humans and animals for prophylactic and therapeutic purposes [72, 73]. Treatment plans are still lacking for patients with respiratory tract viral infections who are not critically sick, particularly those affected by the COVID-19 pandemic. Finding novel antiviral candidates with high activity and low toxicity requires constant screening. In this vein, studies have been done on natural products as well as repurposing current drugs against known or anticipated SARS-CoV-2 protein activities, H5N1, H1N1, and herpes simplex viruses.

Natural remedies are better than synthetic ones because of their superior binding affinity, high efficacy, and lack of side effects. Synthetic pharmaceuticals are highly reactive and may inadvertently affect other human tissues or organs [74]. However, overusing synthetic drugs is riskier than using natural remedies. As a result, this study aimed to assess the antiviral efficacy of a panel of naturally occurring plant VOs against certain respiratory viruses, including herpes simplex virus (HSV) type 1 and avian influenza H5N1, human influenza H1N1, and SARS-CoV-2.

In this work, before assessing the antiviral efficacy of the eight VOs that were chosen for this investigation, we evaluated their cytotoxicity, which is measured in terms of CC_{50} (50% cytotoxic concentration), or the EO concentration that causes a 50% decrease in cell viability. This was conducted to ensure that the EOs are not destructive to host cells at the evaluated concentrations. Viral activity is determined by measuring the amount of EO required to reduce viral infection by 50%, or the IC_{50} . To determine the therapeutic suitability of EO, the antiviral selectivity index (SI) is calculated using the ratio of CC_{50} to IC_{50} [75]. Theoretically, medication would be safer and more effective for a particular viral infection if its SI ratio was higher [76]. According to our study, the therapeutic index for *A. cina* against MDCK cells was the highest one, followed by *P. anisum* and *C. sativum*. In the case of VERO cells, the safest oil was *C. sativum*, followed by *C. sinensis* and *R. officinalis*. The safest oil assessed on VERO E6 cells was *C. sinensis*, followed by *R. officinalis* and *P. anisum*. Selectivity index is a commonly recognized metric for expressing a compound's effectiveness *in vitro* at inhibiting virus multiplication [76]. This was evident from the antiviral outcomes of these VOs; for instance, the VOs of *P. anisum* and *C. sativum* demonstrated antiviral efficacy against H5N1 with IC_{50} values of 7.117 $\mu\text{g/mL}$ and 8.117 $\mu\text{g/mL}$, respectively. As well, the two VOs had

antiviral activity against H1N1 with IC_{50} values of 1.673 $\mu\text{g/mL}$ of *P. anisum* and 13.71 $\mu\text{g/mL}$ of *C. sativum*. This activity matched those documented in the literature. According to a study by GabAllah *et al.*, only anise (*P. anisum*) exhibited substantial antiviral activity against the avian influenza H5N1 virus out of eight aqueous extracts of the Apiaceae family, which included dill, celery, caraway, coriander, cumin, fennel, and anise [77]. The author suggested that the mode of action of this effective anise extract was due to its virucidal effect, as well as its direct effect on the replication of the avian influenza H5N1 virus. Compared to the research conducted by GabAllah *et al.*, the aqueous extracts of the plants that were evaluated showed weaker IC_{50} values than their equivalent VOs in our investigation.

Furthermore, with an IC_{50} of 18.28 $\mu\text{g/mL}$, *P. anisum* demonstrated the highest activity of any VO against HSV. This was in line with a study by Koch *et al.* that demonstrated anise oil had strong antiviral activity against isolates of acyclovir-resistant and acyclovir-sensitive HSV [78]. Additionally, three lignin-carbohydrate-protein complexes, LC1, LC2, and LC3, that were separated from a hot water extract of *P. anisum* seeds had antiviral properties against types 1 and 2 of the HSV [79]. Moreover, *trans*-anethole, which is the major constituent in *P. anisum* VO, was one of six metabolites examined in an *in vitro* study that, at a maximal noncytotoxic concentration, inhibited the HSV-1 infectivity by more than 90% [80]. Also, in another study on star anise oil, which is nearly similar to *P. anisum*, anethole inhibited herpes virus infectivity by more than 90% using an *in vitro* plaque reduction assay.

Additionally, *R. officinalis*, *T. vulgaris*, *C. sinensis*, *P. anisum*, and *C. sativum* exhibited the best inhibitory activity against SARS-CoV-2 with IC_{50} values of 3.07 $\mu\text{g/mL}$, 3.33 $\mu\text{g/mL}$, 3.90 $\mu\text{g/mL}$, 4.66 $\mu\text{g/mL}$, and 4.84 $\mu\text{g/mL}$, respectively. This was agreed with those reported in the literature. In a study done by Zeljković, *et al.*, the compound 1,8-cineol (eucalyptol), which is found in *R. officinalis* VO, was found to be effective in preventing SARS-CoV-2 multiplication in infected cells [81]. Additionally, *in silico* research suggested that 1,8-cineol may possess antiviral capabilities against SARS-CoV-2 [82]. Also, 1,8-cineol, together with the major components in *Laurus nobilis* VO, displayed an intriguing inhibitory effect against SARS-CoV replication ($IC_{50} = 120 \text{ g/mL}$) as a result of their *in vitro* antiviral properties [83]. According to an *in silico* study, 1,8-cineole had the ability to bind with the SARS-CoV-2 major protease and create hydrophobic, ionic, and hydrogen bonding interactions [84]. Furthermore, the *in silico* investigation showed that the compounds thymol, *p*-cymene, carvacrol, γ -terpinene, and linalool, which are prevalent in our prospective VOs, showed anti-SARS-CoV-2 characteristics through ACE2 inhibition [85]. It is noted that the inhibitory concentrations of the eight VOs in our study as anti-SARS-CoV-2 were more potent than those previously reported [81].

Although the paucity of antiviral research focused on particular virus strains as in our study, their results were consistent with other investigations of these oils' antiviral properties. These VOs have been shown to have antiviral efficacy against a variety of viral strains in addition to their effects on H5N1, HSV, H1N1, and SARS-CoV-2 viruses. *P. anisum* demonstrated antiviral activity against dengue virus at concentrations of 200 g/ml to 500 g/ml, which may prevent the virus from reproducing, according to the findings of a study conducted to assess the antiviral activity of *P. anisum* against dengue virus [86]. Also, thirty-four extracts, including those of *P. anisum*, demonstrated considerable inhibitory action greater than 60% at 100 $\mu\text{g/mL}$ during a massive screening in Sudan that examined 152 water and methanol extracts of 71 plants often used in traditional medicine against C virus (HCV) protease [87]. Moreover, *P. anisum* VO demonstrated potent anti-influenza A/WS/33 viral action, which may be attributed to its primary constituents, anethole, estragole, and linalool (82.78%, 8.21%, and 2.74%, respectively) [88]. When rosemary extract (*R. officinalis*) was added at a concentration of 30 $\mu\text{g/mL}$, HSV-1 plaques were inhibited by 55%, while HSV-2 plaques were inhibited by 65%. The extracts, at 50 $\mu\text{g/mL}$, totally prevented the production of HSV-1 and HSV-2 plaques [89]. Moreover, the seed extract of coriander exhibited antiviral activity against the hepatitis A virus [90].

Linalool was a common constituent in the chemical compositions of *C. sativum* and *R. officinalis* VOs as in our study, and was also reported in *P. anisum* VO [88]. According to Choi, Hwa-Jung, *et al.*, linalool may be responsible for the antiviral activity of the *P. anisum* and other plants' VO which also contain linalool as marjoram and sage against the influenza A/WS/33 virus [88]. According to a recent study, the compound dodecanal, which is one of the *C. sativum* oil components, inhibited the growth of several viruses, including the coronavirus responsible for the dengue virus and Middle East respiratory syndrome (MERS) [90]. Also, the compounds decanal, E-2-dodecanol, and E-2-decenol present in *C. sativum* were docked with thirteen proteins of dengue virus as well as the MERS corona via *in silico* methods [91]. The molecular docking results showed that the possible binding modes of these compounds were succeeded with 7 proteins of the dengue virus and 6 proteins of the MERS coronavirus [91].

After screening the eight VOs, three VOs (*C. sativum*, *P. anisum*, and *R. officinalis*) were chosen based on their effectiveness against the tested viral strains. To comprehend potential mechanisms and identify targets of antiviral activity of these oils, we analyzed these VOs using the GC-MS technique to determine their constituents. The composition of these oils was matched with those reported in the literature. In line with our analysis, Salem *et al.*, reported that anethole and himachalene were the major constituents of *P. anisum* VO [47], whereas El-Kersh *et al.* reported that the most prominent constituents in *P. anisum* VO were anethol, pseudoisoeugenol 2-methyl butanoate, himachalene, and thellungianin G [51]. Salem *et al.*, stated that linalool, terpinene, camphor, and alpha-pinene were the major constituents of *C. sativum* VO [47], while Mohamed *et al.* reported that linalool, α -pinene, cymene, estragole, and limonene were the major ones [56], and our analysis agrees with these findings. In line with our study, K. Hussein *et al.* revealed that the main components of *R. officinalis* oil were α -pinene, camphor, eucalyptol, camphene, and D-limonene [92]. Alpha-pinene, eucalyptol, and verbenone were the primary compounds found in rosemary oil, according to a different study presented by G. Mwithiga *et al.*; these findings aligned with our inquiry [93].

Given the widespread interest in finding drugs to combat the COVID-19 pandemic, this study chose to investigate the suggested mechanism of the most potent VOs (*P. anisum*, *C. sativum*, and *R. officinalis*) in conjunction with the main compound in *P. anisum* (anethole) against the molecular targets of SARS-CoV-2, PLpro, ACE2, and spike protein. To

understand the possible mechanism that may contribute to SARS-CoV-2 viral suppression, we must identify the virus's pathways, starting with its attachment to host cells. SARS-CoV-2 mostly infects type II pneumocytes and lymphatic epithelial cells, which trigger the body's innate defense mechanism by releasing interferons (IFNs) [94]. IFN activates the ACE2 protein, which functions as a receptor for viral attachment to host cells. The proteolytic cleavage of the spike (S) protein and ACE2 at the S1-S2 boundary and S2' location is catalyzed by transmembrane protease serine 2 (TMPRSS2). This process further facilitates the fusion of the viral and host cell plasma membranes [94]. The virus's single-stranded RNA is translated by host machinery into viral polypeptides (pp1a and pp1ab), which are subsequently broken down by PLpro and main protease (Mpro) proteins through proteolysis to produce non-structural proteins (Nsps). These Nsps generate a series of subgenomic messenger RNAs via the replication transcription complex (RTC), which is constantly duplicated, that code for structural and auxiliary proteins [94]. Viral genomic RNA and proteins are used to assemble the virus particles in the ER-Golgi intermediate compartment (ERGIC). The virus that is contained in the vesicle subsequently merges with the host's plasma membrane to release the viral particles from the cell. Thus, compounds that break the link between the ACE2 receptor and the SARS-CoV-2 spike protein receptor binding domain protein (RBD) could act as entrance inhibitors [95].

According to the study's findings, *P. anisum*'s VO strongly inhibited the ACE2 spike protein RBD and PLpro enzymes compared to remdesivir and molniravir. This was matched with an *in silico* study reported by Kulkarni *et al.*, in which specific VO compounds from star anise, clove, cinnamon, thyme, holy basil, basil, ajwain, eucalyptus, oregano, and geranium were analyzed against the spike protein. Anethole, carvacrol, cinnamaldehyde, cinnamyl acetate, geraniol, and 1-4-terpineol displayed better binding affinities for the target protein. Hydrophobic interactions and hydrogen bonds stabilized the protein-ligand complexes [22]. Furthermore, compared to the entire volatile oil, the main component of *P. anisum* VO, anethole, displayed less inhibitory activity on these enzymes. This may be explained by the synergistic complex interactions between the various compounds in the entire oil, which result in total inhibition rather than just being caused by anethole. The results given by Ć. Zeljković, *et al.* proved the aforementioned claim, which affirms the efficacy of the entire oil rather than its constituents [81].

P. anisum VO showed 76% spike protein RBD enzyme inhibitory activity, which was the highest percent compared to other VOs or the standard antiviral drugs. This was in accordance with the work presented by Kulkarni *et al.*, who assessed the effectiveness of a range of VOs found in various plant families against the S1 (also known as receptor binding domain, RBD) subunit of spike (S) proteins of SARS-CoV-2. According to the findings, anethole, cinnamaldehyde, carvacrol, geraniol, L-4-terpineol, cinnamoyl acetate, thymol, and pulegone had the strongest ability to inhibit the S1 subunit of S proteins among the assessed VOs [22]. *P. anisum* VO was also the most potent sample, with a percentage up to 76.8% effective against papain-like protease enzyme.

The molecular docking investigation revealed that, in comparison to other selected targets, the main component of *P. anisum* VO, anethole, exhibited a significant binding affinity towards SARS-CoV-2 papain-like protease. Additionally, compared to other major VO components, it demonstrated a distinct binding mechanism against the SARS-CoV-2 spike protein. This was supported by the research conducted by Prabhu, *et al.* which docked the phytochemical components of *C. sativum* against the main protease of SARS-CoV-2. Among the substances under investigation, erucic acid, cosomosiin, rosmarinic, and pimentel seem to have the capacity to block the primary protease of SARS-CoV-2. This could account for the lower activity of linalool, a key component of *C. sativum*, against the specific targets we examined in our study. The ADMET characteristics of the major VO components (anethole, longifolene, α -pinene, camphor, endoborneol, eucalyptol, and linalool) were summarized in Table 10, emphasizing important information of pharmacological significance. All of the investigated compounds from the three potent VOs satisfy Lipinski's five criteria and are good candidates for pharmaceutical drug development due to their favourable pharmacokinetic features, based on the *in-silico* predictions of physicochemical properties.

Based on computational molecular docking, anethole was selected for further analysis using MD simulation in order to assess the flexibility and stability of the protein-ligand complex. Our finding revealed that anethole-SARS-CoV-2 spike, anethole-CoV spike (S) glycoprotein, and anethole-SARS-CoV-2 papain-like protease systems had binding affinities of -21.43 kcal/mol, -21.83 kcal/mol, and -11.15 kcal/mol, respectively. Also, anethole had fitted in the catalytic working site of the SARS-CoV-2 spike and created a Pi-alkyl contact with Leu 73, Val 191, and Val 194. The MD simulation study indicates that anethole binds to the catalytic pocket of the SARS-CoV-2 spike receptor, the CoV spike (S) glycoprotein receptor, and the SARS-CoV-2 papain-like protease with binding affinity, stability, and structural conformation.

Interestingly, the docking data also closely matched the previously mentioned *in vitro* results. The results of this study ultimately highlight the possible antiviral properties of selected natural volatile oils and their main active ingredient against specific respiratory RNA and DNA viruses that have a detrimental effect on public health. The identity of additional antiviral compounds in these oils, their virucidal or inhibitory potential in experimental animals (preclinical studies), and the potential synergistic effects among the active ingredients and effective oils in targeting upper respiratory tract viruses all require more research.

Conclusion

In the present work, we investigated the cytotoxicity and antiviral activity of eight selected volatile oils. The most secure oil on MDCK cells was *Artemisia cina*, followed by *Pimpinella anisum* and *Coriandrum sativum*. In the case of VERO cells, the safest oil was *C. sativum*, followed by *Citrus sinensis* and *Rosmarinus officinalis*. The safest oil assessed on VERO E6 cells against the SARS-CoV-2 virus was *C. sinensis*, followed by *R. officinalis* and *P. anisum*. The VOs of *C. sativum* and *P. anisum* exhibited noticeable antiviral activity against H5N1 and H1N1, while the best one from the tested VOs tested against HSV was *P. anisum*. Almost eight VOs had antiviral activity against SARS-CoV-2. The screening of the eight VOs based on their effectiveness against the tested viral strains led to the selection of three VOs (*C. sativum*, *P. anisum*, and *R. officinalis*). In order to comprehend potential mechanisms and identify targets of antiviral activity of these oils, these VOs were analyzed

using a GC-MS approach to determine their constituents. Linalool, geranyl acetate, and gamma terpenine were the major constituents in *C. sativum*, while anethol and longifolene were more prominent in *P. anisum*. Eucalyptol, camphor, endoborneol, α -pinene were the major compounds in *R. officinalis*. The study chose to investigate the suggested mechanism of the most potent VOs (*P. anisum*, *C. sativum*, and *R. officinalis*) in conjunction with the main compound in *P. anisum* (anethole) against the molecular targets of SARS-CoV-2, PLpro, ACE2, and spike protein due to the widespread interest in finding drugs to combat the COVID-19 pandemic. *P. anisum*'s VO strongly inhibited the ACE2 spike protein RBD and PLpro enzymes compared to remdesivir and molniravir. Furthermore, compared to the entire volatile oil, the main component of *P. anisum* VO, anethole, displayed less inhibitory activity on these enzymes. *P. anisum* VO showed the highest percent spike protein RBD enzyme inhibitory activity, compared to other VOs or the standard antiviral drugs. Additionally, *P. anisum* VO was the most potent VO effective against papain-like protease enzyme. The docking study of the major components of the three selected potent VOs revealed that anethole docked with the receptor in the same pocket as the co-crystallized ligand when docked against SARS-CoV-2 papain-like protease. While in the case of the SARS-CoV-2 spike receptor-binding domain bound with ACE2, anethole docked with the receptor in a hydrophobic-hydrophobic interaction, and the other compounds were clustered in the same cleft. In the case of docking against the SARS-CoV-2 spike receptor, anethole docked with the receptor in a hydrophobic hydrophobic interaction, and other VO's major components were clustered outside the receptor, except for anethole and linalool, which were overlaid and interacted with the same domains inside the receptor. According to the *in-silico* predictions of physicochemical properties, all examined compounds from the three powerful VOs meet Lipinski's five requirements and are suitable candidates for pharmaceutical medication development because of their advantageous pharmacokinetic characteristics. Anethole was selected for analysis using MD simulation to assess the flexibility and stability of the protein-ligand complex. Anethole-SARS-CoV-2 spike, anethole-CoV spike (S) glycoprotein, and anethole-SARS-CoV-2 papain-like protease systems exhibited a noticeable binding affinity. Also, anethole had fitted in the catalytic working site of the SARS-CoV-2 spike and created a Pi-alkyl contact with Leu 73, Val 191, and Val 194. The MD simulation study indicates that anethole binds to the catalytic pocket of the SARS-CoV-2 spike receptor, the CoV spike (S) glycoprotein receptor, and the SARS-CoV-2 papain-like protease with binding affinity, stability, and structural conformation. These results point to a potential application of *P. anisum*, *C. sativum*, and *R. officinalis* VOs as a natural remedy for upper respiratory tract infection caused by DNA or RNA viruses. Future *in vitro* and *in vivo* research to find effective EOs can be supported by our findings, which can also be utilized to direct the development of novel formulations against COVID-19 for a range of food, pharmaceutical, cosmetic, and medical applications. The preclinical and clinical trials of a variety of edible VOs to treat certain respiratory tract illnesses are made possible by this work.

Conflicts of Interests

The authors declare no conflict of interest.

Acknowledgments

The paper was based on work supported by the University of Sadat City (USC) under grant No. (21).

Abbreviations:

ACE2: Angiotensin-converting enzyme 2
BSA: Bovine serum albumin
CPE: Cytopathic effect
DMEM: Dulbecco's Modified Eagle Medium
DTT: Dithiothreitol
EI: Electron ionization
ERGIC: ER-Golgi intermediate compartment
GC-MS: Gas chromatography-mass spectroscopy
H1N1: Influenza A virus
H5N1: Avian influenza A
HRP: horseradish peroxidase
HSV: Herpes simplex virus
IC₅₀: Half-maximal inhibitory concentration
IFNs: Interferons
MDCK: Madin-Darby canine kidney
MERS: Middle East respiratory syndrome
Mpro: Main protease
MTT: 3-(4, 5-dimethylthiazol -2-yl)-2, 5-diphenyltetrazolium bromide
Nsps: Non-structural proteins
PBS: Phosphate buffer saline
PLpro: Papain-like protease
RBD: Receptor binding domain
RTC: Replication transcription complex
SARS-CoV-2: Severe acute respiratory syndrome coronavirus 2
TMB: 3,3',5,5'-Tetramethylbenzidine
TMPRSS2: Transmembrane protease serine 2
VO: Volatile oil

References

- Mizgerd, J.P., *Lung infection--a public health priority*. PLoS Med, 2006. **3**(2): p. e76.
- Safiri, S., A. Mahmoodpoor, A.-A. Kolahi, S.A. Nejadghaderi, M.J. Sullman, M.A. Mansournia, K. Ansarin, G.S. Collins, J.S. Kaufman, and M. Abdollahi, *Global burden of lower respiratory infections during the last three decades*. Frontiers in Public Health, 2023. **10**: p. 1028525.
- World Health Organization. *The top 10 causes of death*. The top 10 causes of death 2024 2/4/2025]; Available from: <https://www.who.int/news-room/fact-sheets/detail/the-top-10-causes-of-death#:~:text=Lower%20respiratory%20infections%20remained%20the,Neonatal%20conditions%20are%20ranked%205th>.
- Tregoning, J.S. and J.r. Schwarze, *Respiratory viral infections in infants: causes, clinical symptoms, virology, and immunology*. Clinical microbiology reviews, 2010. **23**(1): p. 74-98.
- Zaas, A.K., M. Chen, J. Varkey, T. Veldman, A.O. Hero, 3rd, J. Lucas, Y. Huang, R. Turner, A. Gilbert, R. Lambkin-Williams, N.C. Øien, B. Nicholson, S. Kingsmore, L. Carin, C.W. Woods, and G.S. Ginsburg, *Gene expression signatures diagnose influenza and other symptomatic respiratory viral infections in humans*. Cell Host Microbe, 2009. **6**(3): p. 207-17.
- Olenec, J.P., W.K. Kim, W.-M. Lee, F. Vang, T.E. Pappas, L.E.P. Salazar, M.D. Evans, J. Bork, K. Roberg, R.F. Lemanske, and J.E. Gern, *Weekly monitoring of children with asthma for infections and illness during common cold seasons*. Journal of Allergy and Clinical Immunology, 2010. **125**(5): p. 1001-1006.e1.
- Troy, N.M. and A. Bosco, *Respiratory viral infections and host responses; insights from genomics*. Respir Res, 2016. **17**(1): p. 156.
- Yu, H., Y. Shu, S. Hu, H. Zhang, Z. Gao, H. Chen, J. Dong, C. Xu, Y. Zhang, and N. Xiang, *The first confirmed human case of avian influenza A (H5N1) in Mainland China*. The Lancet, 2006. **367**(9504): p. 84.
- Bay, A., Ö. Etlik, A.F. Öner, Ö. Ünal, H. Arslan, A. Bora, R. Davran, S.A. Yuca, and M. Dogan, *Radiological and clinical course of pneumonia in patients with avian influenza H5N1*. European journal of radiology, 2007. **61**(2): p. 245-250.
- Beigel, J.H., J. Farrar, A.M. Han, F.G. Hayden, R. Hyer, M.D. de Jong, S. Lochindarat, T.K. Nguyen, T.H. Nguyen, T.H. Tran, A. Nicoll, S. Touch, and K.Y. Yuen, *Avian influenza A (H5N1) infection in humans*. N Engl J Med, 2005. **353**(13): p. 1374-85.
- Schünemann, H.J., S.R. Hill, M. Kakad, R. Bellamy, T.M. Uyeki, F.G. Hayden, Y. Yazdanpanah, J. Beigel, T. Chotpitayasunondh, C. Del Mar, J. Farrar, T.H. Tran, B. Ozbay, N. Sugaya, K. Fukuda, N. Shindo, L. Stockman, G.E. Vist, A. Croisier, A. Nagjdaliyev, C. Roth, G. Thomson, H. Zucker, and A.D. Oxman, *WHO Rapid Advice Guidelines for pharmacological management of sporadic human infection with avian influenza A (H5N1) virus*. Lancet Infect Dis, 2007. **7**(1): p. 21-31.
- Hopkins, J. *Coronavirus Resource Center*. 2023 24 Jan 2023]; Available from: <https://coronavirus.jhu.edu/map.html>.
- Iqhrammullah, M., D.R. Rizki, A. Purnama, T.F. Duta, H. Harapan, R. Idroes, and B. Ginting, *Antiviral Molecular Targets of Essential Oils against SARS-CoV-2: A Systematic Review*. Scientia Pharmaceutica, 2023. **91**(1): p. 15.
- Hassan, W., S.K. Kazmi, M.J. Tahir, I. Ullah, H.A. Royan, M. Fahriani, F. Nainu, and S.G. Rosa, *Global acceptance and hesitancy of COVID-19 vaccination: A narrative review*. Narra J, 2021.
- Tang, B., X. Zhang, Q. Li, N.L. Bragazzi, D. Golemi-Kotra, and J. Wu, *The minimal COVID-19 vaccination coverage and efficacy to compensate for a potential increase of transmission contacts, and increased transmission probability of the emerging strains*. BMC Public Health, 2022. **22**(1): p. 1258.
- Elsebai, M.F. and M.A. Albalawi, *Essential Oils and COVID-19*. Molecules, 2022. **27**(22).
- Zaman, W., S. Saqib, F. Ullah, A. Ayaz, and J. Ye, *COVID-19: Phylogenetic approaches may help in finding resources for natural cure*. Phytother Res, 2020. **34**(11): p. 2783-2785.
- Horváth, G. and K. Ács, *Essential oils in the treatment of respiratory tract diseases highlighting their role in bacterial infections and their anti-inflammatory action: a review*. Flavour Fragr J, 2015. **30**(5): p. 331-341.
- Ma, L. and L. Yao, *Antiviral Effects of Plant-Derived Essential Oils and Their Components: An Updated Review*. Molecules, 2020. **25**(11).
- Astani, A., J. Reichling, and P. Schnitzler, *Comparative study on the antiviral activity of selected monoterpenes derived from essential oils*. Phytother Res, 2010. **24**(5): p. 673-9.
- Schnitzler, P., *Essential Oils for the Treatment of Herpes Simplex Virus Infections*. Chemotherapy, 2019. **64**(1): p. 1-7.
- Kulkarni, S.A., S.K. Nagarajan, V. Ramesh, V. Palaniyandi, S.P. Selvam, and T. Madhavan, *Computational evaluation of major components from plant essential oils as potent inhibitors of SARS-CoV-2 spike protein*. Journal of Molecular Structure, 2020. **1221**: p. 128823.
- Dutt, J., B. Ganatra, N. Suthar, M. Malek, B. Shukla, K. Shukla, K. Shukla, S. Pandit, M. Rachchh, R. Gokani, and M. Bhalani, *A randomized and comparative study to assess safety and efficacy of supplemental treatment of a herbal formulation - Aayudh Advance comprising essential oils in patients with corona virus 2019 (COVID-19)*. Contemp Clin Trials Commun, 2021. **22**: p. 100755.
- Hawkins, J., C. Hires, L. Keenan, and E. Dunne, *Aromatherapy blend of thyme, orange, clove bud, and frankincense boosts energy levels in post-COVID-19 female patients: A randomized, double-blinded, placebo controlled clinical trial*. Complement Ther Med, 2022. **67**: p. 102823.
- Mohamed, N., N. Baharom, W.S. Wan Sulaiman, Z. Zainol Rashid, K.K.S. Wong, U.K. Ali, S.N. Othman, M.N. ABD SAMAD, N. Kori, P. Periyasamy, N.A. Zakaria, A. Sugumar, N.E. Mohammad Kazmin, X.K. Cheong, S. Saniman, and

- I. Isahak, *early viral clearance among covid-19 patients when gargling with povidone-iodine and essential oils: a pilot clinical trial*. medRxiv, 2020.
26. Refaey, M.S., M.A. Fayed, O. Kutkat, Y. Moatasim, N.S. Tolba, A. Anis, A.M. Elshorbagy, K. Nassar, K.A. Abouzid, and Y.A. Elshaier, *Bio-guided chemical characterization and nano-formulation studies of selected edible volatile oils with potential antibacterial and anti-SARS-CoV-2 activities*. Arabian Journal of Chemistry, 2023. **16**(7): p. 104813.
 27. Refaey, M.S., M.E. Abouelela, E.A. El-Shoura, H.M. Alkhalidi, S.A. Fadil, S.S. Elhady, and R.F. Abdelhameed, *In vitro anti-Inflammatory activity of Cotula anthemoides essential oil and in silico molecular docking of its bioactives*. Molecules, 2022. **27**(6): p. 1994.
 28. Kandeil, A., A. Mostafa, O. Kutkat, Y. Moatasim, A.A. Al-Karmalawy, A.A. Rashad, A.E. Kayed, A.E. Kayed, R. El-Shesheny, and G. Kayali, *Bioactive polyphenolic compounds showing strong antiviral activities against severe acute respiratory syndrome coronavirus 2*. Pathogens, 2021. **10**(6): p. 758.
 29. Mostafa, A., A. Kandeil, Y. AMM Elshaier, O. Kutkat, Y. Moatasim, A.A. Rashad, M. Shehata, M.R. Gomaa, N. Mahrous, and S.H. Mahmoud, *FDA-approved drugs with potent in vitro antiviral activity against severe acute respiratory syndrome coronavirus 2*. Pharmaceuticals, 2020. **13**(12): p. 443.
 30. Kutkat, O., A. Kandeil, Y. Moatasim, Y.A. Elshaier, W.A. El-Sayed, S.T. Gaballah, A. El Taweel, M.N. Kamel, M. El Sayes, and M.A. Ramadan, *In Vitro and in vivo antiviral studies of new heteroannulated 1, 2, 3-Triazole glycosides targeting the neuraminidase of influenza A viruses*. Pharmaceuticals, 2022. **15**(3): p. 351.
 31. Tai, W., L. He, X. Zhang, J. Pu, D. Voronin, S. Jiang, Y. Zhou, and L. Du, *Characterization of the receptor-binding domain (RBD) of 2019 novel coronavirus: implication for development of RBD protein as a viral attachment inhibitor and vaccine*. Cellular & molecular immunology, 2020. **17**(6): p. 613-620.
 32. Abomughaid, M.M., M.S. Nofal, K.I. Ghaleb, M.G. Seadawy, M.G. Abdel-Wahab, A.S. Hegazy, and D.A. Ghareeb, *ZnO-chlorogenic acid nanostructured complex inhibits Covid-19 pathogenesis and increases hydroxychloroquine efficacy*. Journal of King Saud University-Science, 2022. **34**(8): p. 102296.
 33. Ghareeb, D.A., S.R. Saleh, M.G. Seadawy, M.S. Nofal, S.A. Abdulmalek, S.F. Hassan, S.M. Khedr, M.G. Abdelwahab, A.A. Sobhy, and A.s.A. Abdel-Hamid, *Nanoparticles of ZnO/Berberine complex contract COVID-19 and respiratory co-bacterial infection in addition to elimination of hydroxychloroquine toxicity*. Journal of Pharmaceutical Investigation, 2021. **51**: p. 735-757.
 34. Hospital, A., J.R. Goñi, M. Orozco, and J.L. Gelpi, *Molecular dynamics simulations: advances and applications*. Advances and Applications in Bioinformatics and Chemistry, 2015: p. 37-47.
 35. Lee, T.-S., D.S. Cerutti, D. Mermelstein, C. Lin, S. LeGrand, T.J. Giese, A. Roitberg, D.A. Case, R.C. Walker, and D.M. York, *GPU-accelerated molecular dynamics and free energy methods in Amber18: performance enhancements and new features*. Journal of chemical information and modeling, 2018. **58**(10): p. 2043-2050.
 36. Wang, J., W. Wang, P.A. Kollman, and D.A. Case, *Automatic atom type and bond type perception in molecular mechanical calculations*. Journal of molecular graphics and modelling, 2006. **25**(2): p. 247-260.
 37. Berendsen, H.J., J.v. Postma, W.F. Van Gunsteren, A. DiNola, and J.R. Haak, *Molecular dynamics with coupling to an external bath*. The Journal of chemical physics, 1984. **81**(8): p. 3684-3690.
 38. Roe, D.R. and T.E. Cheatham III, *PTRAJ and CPPTRAJ: software for processing and analysis of molecular dynamics trajectory data*. Journal of chemical theory and computation, 2013. **9**(7): p. 3084-3095.
 39. Seifert, E., *OriginPro 9.1: scientific data analysis and graphing software-software review*. Journal of chemical information and modeling, 2014. **54**(5): p. 1552.
 40. Pettersen, E.F., T.D. Goddard, C.C. Huang, G.S. Couch, D.M. Greenblatt, E.C. Meng, and T.E. Ferrin, *UCSF Chimera—a visualization system for exploratory research and analysis*. Journal of computational chemistry, 2004. **25**(13): p. 1605-1612.
 41. Hayes, J.M. and G. Archontis, *MM-GB (PB) SA calculations of protein-ligand binding free energies*. Molecular dynamics-studies of synthetic and biological macromolecules, 2012: p. 171-190.
 42. Ylilauri, M. and O.T. Pentikäinen, *MMGBSA as a tool to understand the binding affinities of filamin-peptide interactions*. Journal of chemical information and modeling, 2013. **53**(10): p. 2626-2633.
 43. Kollman, P.A., I. Massova, C. Reyes, B. Kuhn, S. Huo, L. Chong, M. Lee, T. Lee, Y. Duan, and W. Wang, *Calculating structures and free energies of complex molecules: combining molecular mechanics and continuum models*. Accounts of chemical research, 2000. **33**(12): p. 889-897.
 44. Hou, T., J. Wang, Y. Li, and W. Wang, *Assessing the performance of the MM/PBSA and MM/GBSA methods. 1. The accuracy of binding free energy calculations based on molecular dynamics simulations*. Journal of chemical information and modeling, 2011. **51**(1): p. 69-82.
 45. Greenidge, P.A., C. Kramer, J.-C. Mozziconacci, and R.M. Wolf, *MM/GBSA binding energy prediction on the PDBbind data set: successes, failures, and directions for further improvement*. Journal of chemical information and modeling, 2013. **53**(1): p. 201-209.
 46. Sitkoff, D., K.A. Sharp, and B. Honig, *Accurate calculation of hydration free energies using macroscopic solvent models*. The Journal of Physical Chemistry, 1994. **98**(7): p. 1978-1988.
 47. Salem, M.A., E.G. Manaa, N. Osama, N.M. Aborehab, M.F. Ragab, Y.A. Haggag, M.T. Ibrahim, and D.I. Hamdan, *Coriander (Coriandrum sativum L.) essential oil and oil-loaded nano-formulations as an anti-aging potentiality via TGFβ/SMAD pathway*. Scientific reports, 2022. **12**(1): p. 6578.
 48. Ali, M., A. Mujib, B. Gulzar, and N. Zafar, *Essential oil yield estimation by Gas chromatography–mass spectrometry (GC–MS) after Methyl jasmonate (MeJA) elicitation in in vitro cultivated tissues of Coriandrum sativum L.* 3 Biotech, 2019. **9**: p. 1-16.

49. Czerwik-Marcinkowska, J., *ESSENTIAL OIL COMPOSITION OF THE CORIANDER (Coriandrum sativum L.) HERB DEPENDING ON THE DEVELOPMENT STAGE*. Acta Agrobotanica, 2013. **66**(1).
50. Haşimi, N., V. Tolan, S. KIZIL, and E. KILINÇ, *Anason (Pimpinella anisum L.) ve kimyon (Cuminum cyminum) tohumlarının uçucu yağ içeriği, antimikrobiyal ve antioksidan özelliklerinin belirlenmesi*. Journal of Agricultural Sciences, 2014. **20**(1): p. 19-26.
51. El-Kersh, D.M., N.M. Mostafa, S. Fayez, T. Al-Warhi, M.A. Abourehab, W.M. Eldehna, and M.A. Salem, *GC-MS metabolites profiling of anethole-rich oils by different extraction techniques: antioxidant, cytotoxicity and in-silico enzymes inhibitory insights*. Journal of Enzyme Inhibition and Medicinal Chemistry, 2022. **37**(1): p. 1974-1986.
52. Mohammed, M.J. and H.A. Ebraheem, *Gas Chromatography-Mass Spectrometry Profiling of Pimpinella anisum Oils and its Antimicrobial and Antioxidant Activities*.
53. Hussein, K.A., Y.D. Lee, and J.H. Joo, *Effect of rosemary essential oil and Trichoderma koningiopsis VOCs on pathogenic fungi responsible for ginseng root-rot disease*. 2020.
54. Mwithiga, G., S. Maina, J. Gitari, and P. Muturi, *Rosemary (Rosmarinus officinalis L.) growth rate, oil yield and oil quality under differing soil amendments*. Heliyon, 2022. **8**(4): p. e09277.
55. Mazza, G., *Minor volatile constituents of essential oil and extracts of coriander (Coriandrum sativum L.) fruits*. Sciences des aliments, 2002. **22**(5): p. 617-627.
56. Mohamed, M., M. Ibrahim, and H. Wahba, *Flavoring compounds of essential oil isolated from agriculture waste of coriander (Coriandrum sativum) plant*. J. Mater. Environ. Sci, 2018. **9**(1): p. 77-82.
57. Calleja, D.J., N. Kuchel, B.G. Lu, R.W. Birkinshaw, T. Klemm, M. Doerflinger, J.P. Cooney, L. Mackiewicz, A.E. Au, and Y.Q. Yap, *Insights Into Drug Repurposing, as Well as Specificity and Compound Properties of Piperidine-Based SARS-CoV-2 PLpro Inhibitors*. Frontiers in chemistry, 2022. **10**: p. 328.
58. Lan, J., J. Ge, J. Yu, S. Shan, H. Zhou, S. Fan, Q. Zhang, X. Shi, Q. Wang, and L. Zhang, *Structure of the SARS-CoV-2 spike receptor-binding domain bound to the ACE2 receptor*. nature, 2020. **581**(7807): p. 215-220.
59. Wrapp, D., N. Wang, K. Corbett, J. Goldsmith, C. Hsieh, O. Abiona, B. Graham, and J. McLellan, *Prefusion 2019-nCoV spike glycoprotein with a single receptor-binding domain up*. Science, 2020. **367**(6483): p. 1260-1263.
60. Molsoft. *Drug-Likeness and molecular property prediction*. 2024 [accessed 8/2/2024]; Available from: <https://molsoft.com/mprop/>.
61. PreADMET. *ADME Prediction*. 2023 [accessed 23/12/2023]; Available from: <https://preadmet.webservice.bmdrc.org/>.
62. Ames, B.N., E. Gurney, J.A. Miller, and H. Bartsch, *Carcinogens as frameshift mutagens: metabolites and derivatives of 2-acetylaminofluorene and other aromatic amine carcinogens*. Proceedings of the National Academy of Sciences, 1972. **69**(11): p. 3128-3132.
63. Mirzaei, S., F. Eisvand, F. Hadizadeh, F. Mosaffa, A. Ghasemi, and R. Ghodsi, *Design, synthesis and biological evaluation of novel 5, 6, 7-trimethoxy-N-aryl-2-styrylquinolin-4-amines as potential anticancer agents and tubulin polymerization inhibitors*. Bioorganic Chemistry, 2020. **98**: p. 103711.
64. Hasanin, M., A.H. Hashem, A.A. El-Rashedy, and S. Kamel, *Synthesis of novel heterocyclic compounds based on dialdehyde cellulose: characterization, antimicrobial, antitumor activity, molecular dynamics simulation and target identification*. Cellulose, 2021. **28**: p. 8355-8374.
65. Machaba, K.E., N.N. Mhlongo, and M.E. Soliman, *Induced mutation proves a potential target for TB therapy: a molecular dynamics study on LprG*. Cell Biochemistry and Biophysics, 2018. **76**: p. 345-356.
66. Pan, L. and J.C. Patterson, *Molecular dynamics study of Zn ($\alpha\beta$) and Zn ($\alpha\beta$) 2*. PLoS One, 2013. **8**(9): p. e70681.
67. Wijffels, G., B. Dalrymple, K. Kongsuwan, and N.E. Dixon, *Conservation of eubacterial replicases*. IUBMB life, 2005. **57**(6): p. 413-419.
68. Richmond, T.J., *Solvent accessible surface area and excluded volume in proteins: Analytical equations for overlapping spheres and implications for the hydrophobic effect*. Journal of molecular biology, 1984. **178**(1): p. 63-89.
69. Papadourakis, M., H. Sinenka, P. Matricon, J. Hénin, G. Brannigan, L. Pérez-Benito, V. Pande, H. van Vlijmen, C. de Graaf, and F. Deflorian, *Alchemical Free Energy Calculations on Membrane-Associated Proteins*. Journal of Chemical Theory and Computation, 2023. **19**(21): p. 7437-7458.
70. Nassar, A.-E.F., A.M. Kamel, and C. Clarimont, *Improving the decision-making process in the structural modification of drug candidates: enhancing metabolic stability*. Drug discovery today, 2004. **9**(23): p. 1020-1028.
71. Huang, Y., C. Yang, X.-f. Xu, W. Xu, and S.-w. Liu, *Structural and functional properties of SARS-CoV-2 spike protein: potential antiviral drug development for COVID-19*. Acta Pharmacologica Sinica, 2020. **41**(9): p. 1141-1149.
72. El-Shesheny, R., O. Bagato, A. Kandeil, A. Mostafa, S.H. Mahmoud, H.M. Hassanneen, R.J. Webby, M.A. Ali, and G. Kayali, *Re-emergence of amantadine-resistant variants among highly pathogenic avian influenza H5N1 viruses in Egypt*. Infection, Genetics and Evolution, 2016. **46**: p. 102-109.
73. Kumar, M., K. Kuroda, K. Dhangar, P. Mazumder, C. Sonne, J. Rinklebe, and M. Kitajima, *Potential emergence of antiviral-resistant pandemic viruses via environmental drug exposure of animal reservoirs*. Environmental science & technology, 2020. **54**(14): p. 8503-8505.
74. Farooq, S. and Z. Ngaini, *Natural and synthetic drugs as potential treatment for coronavirus disease 2019 (COVID-2019)*. Chemistry Africa, 2021. **4**(1): p. 1-13.
75. Pilau, M.R., S.H. Alves, R. Weiblen, S. Arenhart, A.P. Cueto, and L.T. Lovato, *Antiviral activity of the Lippia graveolens (Mexican oregano) essential oil and its main compound carvacrol against human and animal viruses*. Brazilian Journal of Microbiology, 2011. **42**: p. 1616-1624.
76. Flamand, L., I. Lautenschlager, G. Krueger, and D. Ablashi, *Human Herpesviruses HHV-6A, HHV-6B and HHV-7: diagnosis and clinical management*. Vol. 12. 2014: Elsevier.

77. GabAllah, M., A. Kandeil, A.E.-B. Mousa, and M. Ahmed Ali, *Antiviral activity of water extracts of some medicinal and nutritive plants from the Apiaceae family*. Novel Research in Microbiology Journal, 2020. **4**(2): p. 725-735.
78. Koch, C., J. Reichling, R. Kehm, M.M. Sharaf, H. Zentgraf, J. Schneelee, and P. Schnitzler, *Efficacy of anise oil, dwarf-pine oil and chamomile oil against thymidine-kinase-positive and thymidine-kinase-negative herpesviruses*. Journal of Pharmacy and Pharmacology, 2008. **60**(11): p. 1545-1550.
79. Lee, J.-B., C. Yamagishi, K. Hayashi, and T. Hayashi, *Antiviral and immunostimulating effects of lignin-carbohydrate-protein complexes from Pimpinella anisum*. Bioscience, biotechnology, and biochemistry, 2011. **75**(3): p. 459-465.
80. Astani, A., J. Reichling, and P. Schnitzler, *Screening for antiviral activities of isolated compounds from essential oils*. Evidence-Based complementary and alternative medicine, 2011. **2011**(1): p. 253643.
81. Ćavar Zeljković, S., E. Schädich, P. Džubák, M. Hajdúch, and P. Tarkowski, *Antiviral activity of selected lamiaceae essential oils and their monoterpenes against SARS-CoV-2*. Frontiers in Pharmacology, 2022: p. 1589.
82. Da Silva, J.K.R., P.L.B. Figueiredo, K.G. Byler, and W.N. Setzer, *Essential oils as antiviral agents, potential of essential oils to treat SARS-CoV-2 infection: an in-silico investigation*. International journal of molecular sciences, 2020. **21**(10): p. 3426.
83. Elsebai, M.F. and M.A. Albalawi, *Essential Oils and COVID-19*. Molecules, 2022. **27**(22): p. 7893.
84. Wani, A.R., K. Yadav, A. Khursheed, and M.A. Rather, *An updated and comprehensive review of the antiviral potential of essential oils and their chemical constituents with special focus on their mechanism of action against various influenza and coronaviruses*. Microbial Pathogenesis, 2021. **152**: p. 104620.
85. Abdelli, I., F. Hassani, S. Bekkel Briki, and S. Ghalem, *In silico study the inhibition of angiotensin converting enzyme 2 receptor of COVID-19 by Ammoides verticillata components harvested from Western Algeria*. Journal of Biomolecular Structure and Dynamics, 2021. **39**(9): p. 3263-3276.
86. Al-Bayaty, F., M.M.J. Al-Obaidi, M.H. Al-Doori, and O. Imad, *ANTI-VIRAL RESEARCH*. 2023.
87. Soussi, M., W. El Yaagoubi, H. Nekhla, L. El Hanafi, W. Squalli, M. Benjelloun, and L. El Ghadraoui, *A multidimensional review of Pimpinella anisum and recommendation for future research to face adverse climatic conditions*. Chemistry Africa, 2023. **6**(4): p. 1727-1746.
88. Choi, H.-J., *Chemical constituents of essential oils possessing anti-influenza A/WS/33 virus activity*. Osong public health and research perspectives, 2018. **9**(6): p. 348.
89. Al-Megrin, W.A., N.A. AlSadhan, D.M. Metwally, R.A. Al-Talhi, M.F. El-Khadragy, and L.J. Abdel-Hafez, *Potential antiviral agents of Rosmarinus officinalis extract against herpes viruses 1 and 2*. Bioscience reports, 2020. **40**(6): p. BSR20200992.
90. Dissanayake, K., W. Fernando, and W. Perera, *Investigation of the phytochemistry of Coriandrum sativum to combat against viral infections*. International Journal of Innovative Pharmaceutical Sciences and Research, 2020. **8**(6): p. 1-10.
91. Rao, S.V., D. Tulasi, K. Pavithra, R. Nisha, and R. Taj, *In silico studies on dengue and MERS coronavirus proteins with selected Coriandrum sativum l. herb constituents*. World J. Pharm. Pharmaceut. Sci, 2018. **7**(12): p. 1-20.
92. Hussein, K.A., Y.-D. Lee, and J.H. Joo, *Effect of rosemary essential oil and Trichoderma koningiopsis T-403 VOCs on pathogenic fungi responsible for ginseng root rot disease*. Journal of Microbiology and Biotechnology, 2020. **30**(7): p. 1018.
93. Mwithiga, G., S. Maina, J. Gitari, and P. Muturi, *Rosemary (Rosmarinus officinalis L.) growth rate, oil yield and oil quality under differing soil amendments*. Heliyon, 2022. **8**(4).
94. Yan, W., Y. Zheng, X. Zeng, B. He, and W. Cheng, *Structural biology of SARS-CoV-2: open the door for novel therapies*. Signal transduction and targeted therapy, 2022. **7**(1): p. 26.
95. Day, C.J., B. Bailly, P. Guillon, L. Dirr, F.E.-C. Jen, B.L. Spillings, J. Mak, M. von Itzstein, T. Haselhorst, and M.P. Jennings, *Multidisciplinary approaches identify compounds that bind to human ACE2 or SARS-CoV-2 spike protein as candidates to block SARS-CoV-2-ACE2 receptor interactions*. MBio, 2021. **12**(2): p. e03681-20.